Pyroxenite xenoliths from the Rio Puerco volcanic field, New Mexico: Melt metasomatism at the margin of the Rio Grande rift

Courtney Porreca
Jane Selverstone*
Kimberly Samuels
Department of Earth & Planetary Sciences, MSC03 2040, University of New Mexico, Albuquerque, New Mexico 87131-0001, USA

ABSTRACT

Mantle xenoliths from the Pliocene Rio Puerco volcanic field, New Mexico, record chemical modification of the subcontinental lithosphere in the transition zone between the Colorado Plateau and the Rio Grande rift. The Rio Puerco necks brought a wide variety of mantle xenoliths to the surface, including abundant spinel ± garnet pyroxenites. Garnet pyroxenites equilibrated at pressures within the spinel lherzolite stability field (16–18 kbar) but at higher temperatures (1020–1100 °C) than lherzolite xenoliths (900–1000 °C). Calcite-bearing pyroxenites record temperatures as high as 1145 °C. Textural observations combined with the high equilibration temperatures are consistent with pyroxenite formation in response to melt interaction with a lherzolite precursor in the approximate ratio of 35% lherzolite to 65% melt. Bulk chemical data and the presence of both carbonatitic and basaltic glass inclusions indicate that the infiltrating melt(s) included both carbonatite and silicate components. Different mantle xenolith populations in volcanic centers of different ages in the Rio Grande rift constrain the likely age of melt infiltration and pyroxenite formation beneath the Puerco necks to Miocene–early Pliocene. Orthopyroxene + spinel + clinopyroxene + silicate glass symplectites around relict garnets record continued rift-related decompression ± heating following pyroxenite formation. Carbonatite + silicate melt generation was likely concentrated in areas affected by earlier metasomatism related to devolatilization of the subducted Farallon slab. Deep-seated fractures associated with the Jemez Lineament may have focused melts beneath the Puerco necks and resulted in wholesale conversion of lherzolite into pyroxenite.

Keywords: metasomatism, pyroxenite, xenolith, Rio Grande rift.

INTRODUCTION

Mantle xenoliths have long been used to document the composition, physical properties, and tectonic evolution of the subcontinental lithosphere beneath the western United States. Most of these studies have focused on various types of olivine-bearing nodules, but many have also noted the presence of pyroxenites. In general, pyroxenites appear to be most prevalent in xenolith suites from the extended lithosphere of the Basin and Range Province, eastern Sierra Nevada, Arizona Transition Zone, and southern Rio Grande rift (Wilshire et al., 1988; Ducea and Saleeby, 1996; McGuire and Mukasa, 1997). Xenolith suites from the Colorado Plateau also contain pyroxenites, but in lesser abundance (McGetchin and Silver, 1972; Wilshire et al., 1988). The association of pyroxenites with regions of extension suggests a genetic link between asthenospheric upwelling and pervasive development of mantle pyroxenites.

Mantle pyroxenites have been proposed as possible source rocks involved in generation of both alkalic basalts (Carlson and Nowell, 2001; Hirschmann et al., 2003; Kogiso et al., 2003) and mid-ocean-ridge basalts (Hirschmann and Stolper, 1996). However, the processes by which the pyroxenites themselves form are not well understood. End-member models fall into several distinct categories; pyroxenites might represent: preserved remnants of subducted oceanic crust mixed into the mantle or melts derived from such material (Xu, 2002; Pearson and Nowell, 2004), primary melt compositions that crystallized within the upper mantle (Ho et al., 2000), cumulates derived from alkali basaltic magmas (McGuire and Mukasa, 1997;

Litasov et al., 2000; Dobosi et al., 2003; Lee et al., 2006), metasomatic rocks that resulted from interaction of reactive fluids and/or melts with mantle peridotites (Irving, 1980; Wilshire et al., 1988; Mukhopadhyay and Manton, 1994; Garrido and Bodinier, 1999; Liu et al., 2005), or some combination of these models (Downes, 2001; Sen et al., 2005).

Several types of pyroxenite xenoliths, along with spinel lherzolites and harzburgites, were brought to the surface in abundance by the Rio Puerco volcanic necks in northwestern New Mexico. These volcanic necks are located in the transition zone between the Colorado Plateau and the extended lithosphere of the Rio Grande rift, a region where physical and chemical modification of the uppermost mantle is likely to have occurred since the onset of rifting. We use textural and chemical data to evaluate models for the formation of the pyroxenites. The pyroxenite samples preserve a more extensive reaction history than is evident in associated lherzolites and, hence, are particularly useful for examining the thermal and chemical modification history of the upper mantle during Rio Grande rifting. Primary mantle carbonates are also present in many of the pyroxenites and provide direct evidence for rock interaction with fluid and/or melt at depth in the mantle.

GEOLOGIC SETTING OF THE RIO PUERCO VOLCANIC NECKS

The xenoliths for this study come from Cenozoic volcanic necks in the Rio Puerco drainage of west-central New Mexico (Fig. 1). The ~50 volcanic necks of the Rio Puerco volcanic field are small-volume, mafic plugs composed of alkaline basalts and volcanic breccias that are part of the adjacent Mt. Taylor volcanic field (Kudo et al., 1972; Hallett, 1994; Hallett et al., 1997). The xenolith-bearing basalts have been dated at 4.49–2.05 Ma (Hallett et al., 1997), and the Mt. Taylor volcanics are comparable in age

*Corresponding author: selver@unm.edu; phone: +1-505-277-6528, fax: +1-505-277-8843.
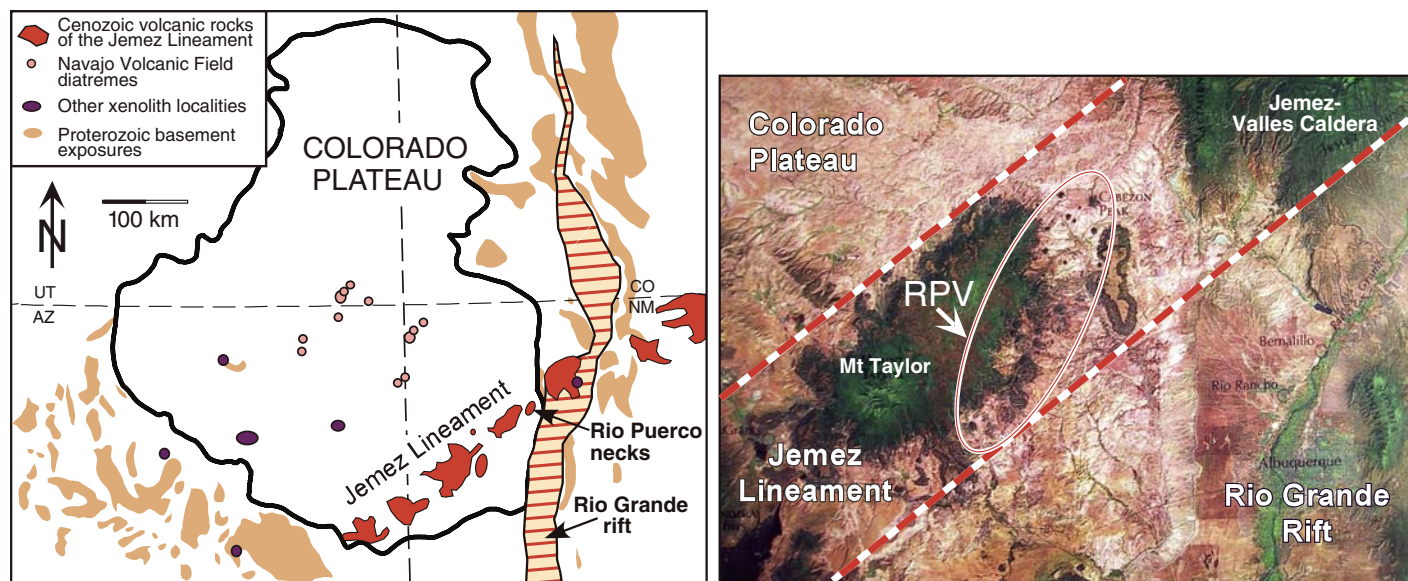
Figure 1. Generalized map and satellite image showing location of the Rio Puerco volcanic (RPV) necks relative to the Colorado Plateau, the Rio Grande rift, and the Jemez Lineament (satellite image excerpted from Resource Map 23 from the New Mexico Bureau of Mining and Mineral Resources, 2000).
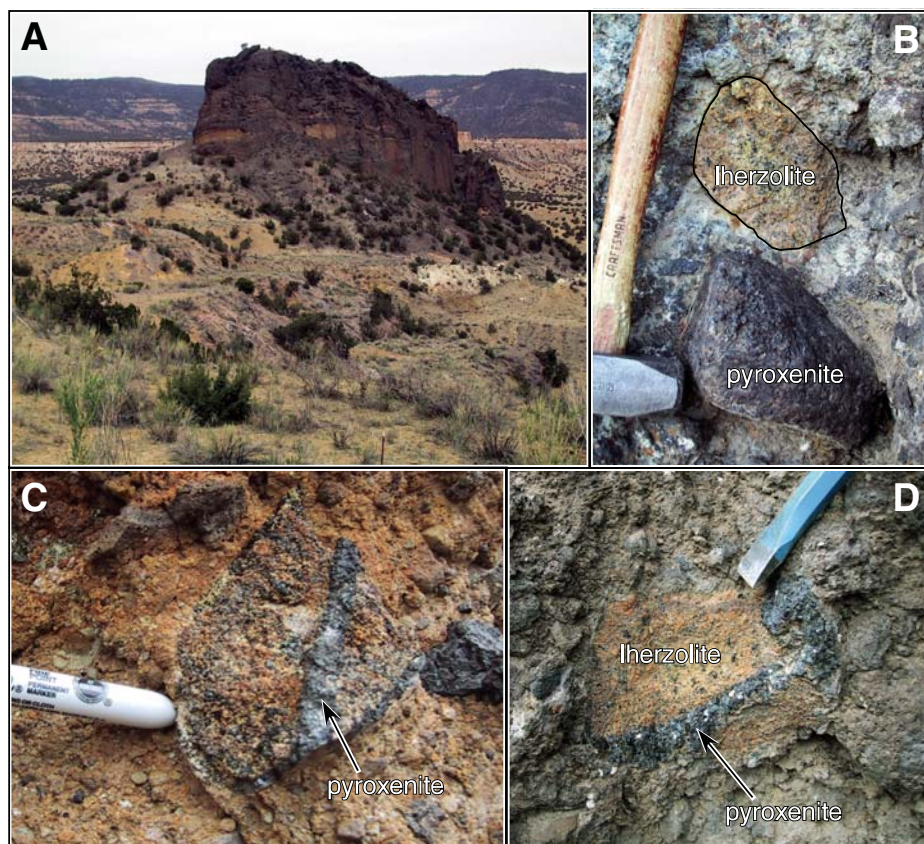

Figure 2. Photos from Cerrito Negro. (A) Prominent banding reflects different pyroclastic eruptions at the neck. (B) Lherzolite and spinel pyroxenite xenoliths enclosed within pyroclastic breccia. (C–D) Composite lherzolite-pyroxenite xenoliths.

at 3.0–1.5 Ma (Perry et al., 1990; Hallett et al., 1997). Both the Rio Puerco and Mt. Taylor volcanic fields occur within the Jemez Lineament, a NE-trending zone of late Tertiary–Quaternary volcanic centers that extends from southwestern Arizona to northeastern New Mexico (Mayo, 1958; Aldrich and Laughlin, 1984). The lineament corresponds to the tectono-physiographic transition zone that separates the thick lithosphere of the southeastern Colorado Plateau from the extended lithosphere of the western margin of the Rio Grande rift and the southeastern Basin and Range Province.

Extension began in the southern portion of the Rio Grande rift around 30 Ma and propagated northward. Volcanism in the rift has been intermittent since the Tertiary, and basalt compositions reflect transition from a lithospheric to an asthenospheric source driven by lithospheric thinning (Perry et al., 1988; Baldridge et al., 1991). This transition in source regions occurred at ca. 10 Ma in the southern part of the rift and in the last 4 m.y. in the central rift on the basis of ε_{Nd} and $^{87}Sr/^{86}Sr$ ratios (McMillan et al., 2000).

The onset of Rio Grande rift extension may have been initiated by the removal of the east-dipping Farallon slab (Dickinson and Snyder, 1978; Humphreys, 1995; Keller and Baldridge, 1999). Low-angle subduction of the Farallon slab, possibly in contact with the base of the lithosphere under the western United States, resulted in cooling and hydration of the North American lithosphere (Coney and Reynolds, 1977; Riter and Smith, 1996; Smith

et al., 1999, 2004; Humphreys et al., 2003). Slab removal likely occurred between 50 and 20 Ma, based on the ages of mantle-derived volcanism thought to have resulted from slab breakoff (Humphreys, 1995).

The Rio Puerco volcanic necks obliquely span the width of the Jemez Lineament and provide an opportunity to examine the mantle lithosphere beneath this feature. Some workers have argued that the lineament is coincident with a Proterozoic province boundary at depth (Karlstrom and Humphreys, 1998; Shaw and Karlstrom, 1999), which may have been reactivated during subsequent tectonism (Dickinson and Snyder, 1978; Humphreys, 1995; Keller and Baldridge, 1999). Seismic data support a deep-rooted structure beneath the lineament (Humphreys and Dueker, 1994; Dueker et al., 2001; Gao et al., 2004), but the physical and chemical significance of the lineament at depth remains unknown.

The LA RISTRA passive seismic line places important constraints on the structure of the upper mantle in this region. West et al. (2004) documented lithospheric thicknesses ranging from 200 km in the Great Plains to 45–55 km beneath the Rio Grande rift and 120–150 km for the Colorado Plateau and argued that slow seismic velocities beneath the rift indicate the presence of partial melt. Gao et al. (2004) attributed a fast anomaly below the Colorado Plateau to the foundering Farallon slab and a slow anomaly just to the east of the plateau as upwelling asthenosphere associated with volatiles released from the slab.

SAMPLE DESCRIPTION AND MINERAL CHEMISTRY

We collected more than 500 xenoliths from 11 of the roughly 50 volcanic necks in the Rio Puerco area. The xenoliths range from 2 to 30 cm in diameter and are found within basaltic plugs, dikes, and tuff rings. The mantle xenolith suite is dominated by spinel lherzolites and pyroxenites, with rare harzburgites, dunites, and megacrysts of spinel and pyroxene. An unusual feature of this xenolith suite is the presence of apparently primary mantle carbonate in many of the samples (Perkins et al., 2006).

In this paper, we focus primarily on xenoliths from the volcanic neck of Cerrito Negro (CTON, Fig. 2A), but also include data from other necks within the volcanic field. Cerrito Negro is dominated by pyroclastic breccia that contains abundant lherzolite and pyroxenite xenoliths (Fig. 2B) in addition to bombs, scoria, and inclusions of the underlying sedimentary country rock (Hallett, 1994). Pristine pyroxenite xenoliths up to 30 cm in diameter weather free of the breccia and display well-rounded and polished surfaces. Although pyroxenites are common at many of the Puerco necks, Cerrito Negro is the only neck at which we found garnet pyroxenites. Several composite lherzolite-pyroxenite xenoliths are exposed in situ within the breccia (Figs. 2C and 2D), although we were unable to obtain intact samples of these xenoliths due to their weathered condition. In all cases where crosscutting relationships are apparent in the composite xenoliths in outcrop, spinel pyroxenite crosscuts lherzolite. However, the contacts between pyroxenite and lherzolite are typically gradational over a distance of millimeters to a few centimeters, suggesting considerable interaction between the two rock types and/or formation of the pyroxenites by reaction between lherzolite and melt/fluid of a different composition. There is no obvious spatial association between pyroxenite in composite xenoliths and the surrounding host basalt.

Mineral and melt inclusion compositions were determined using the JEOL 8200 electron microprobe at the Department of Earth and Planetary Sciences at the University of New Mexico. Quantitative data for this study were obtained from 16 samples. Samples were analyzed with an accelerating voltage of 15 kV, beam diameter of 1 μm, and a beam current of 20 nA. All iron was analyzed as FeO and recalculated for thermobarometric calculations using the method of Droop (1987).

Spinel Lherzolite

Most of the lherzolite samples from the pyroclastic breccia at Cerrito Negro are extensively weathered, and we thus included representative lherzolites from basalts at Cerro de Guadalupe (e.g., CG-38 in Fig. 3), Cerro de Santa Rosa, and Cerro Negro in this study. Lherzolites from
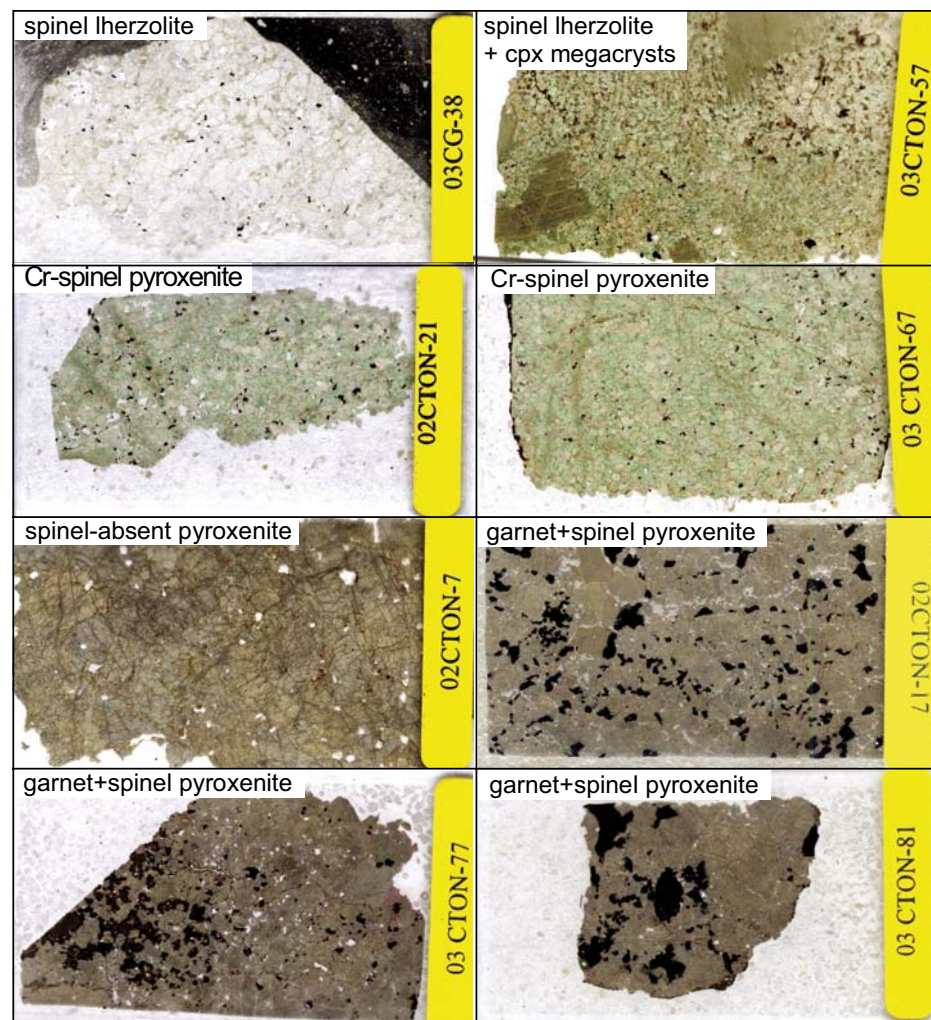

Figure 3. Thin section scans of representative lherzolite and pyroxenite xenoliths. Long dimension of each thin section is 45 mm (cpx—clinopyroxene).

all four necks show a large degree of grain-size heterogeneity. Most samples lack an obvious shear foliation, but deformation lamellae are ubiquitous in olivine, and orthopyroxene generally shows undulose extinction and local subgrain development. A foliation defined by a shape-preferred olivine and pyroxene fabric and by spinel-rich layers is present in a few samples. Several samples, such as CTON-57 (Fig. 3), contain large pyroxene megacrysts with coarse exsolution lamellae that are set in a fine-grained lherzolite matrix. Carbonate is locally present along grain boundaries and in melt pockets within lherzolite samples.

Orthopyroxene is more abundant than clinopyroxene in most lherzolite samples, suggesting that most samples experienced at least some partial melting and melt removal. Exsolution lamellae in the pyroxenes range from very

fine to coarse (<10–100 μm) within the same sample. Fine lamellae are typically confined to the interiors of subhedral orthopyroxene grains and do not extend to the rims of the grains. In most samples, brown spinels are either optically homogeneous or are zoned toward opaque rims. A few samples, however, display narrow symplectitic rims composed of olivine, pyroxene, and plagioclase around spinel. Phlogopite occurs in several lherzolite samples, generally as inclusions within pyroxene. Calcite occurs along grain boundaries and associated with melt pockets in a few samples. Fluid and melt inclusions are locally present along healed fractures within the lherzolites.

Clinopyroxene is dominantly Cr-rich diopside with 5–6 wt% Al_2O_3, 6–14 mol% jadeite component, Mg numbers of 88–94, and low TiO_2 contents (<0.18 wt%) (Figs. 4 and 5).

Orthopyroxene is enstatite with 4–5 mol% Mg-Tschermak component, 0.5–0.6 wt% Cr_2O_3, and Mg numbers of 89–91 (Fig. 4). Megacrystic pyroxenes are similar in composition to finer-grained, matrix pyroxenes (e.g., Fig. 4). Brown, Cr-rich spinel is ubiquitous in the lherzolites. Cr/Cr + Al ratios range from 0.17 to 0.28, with little to no compositional variability within a single sample. Mg numbers in spinel range from 0.70 to 0.75 but show no variation within individual samples. Olivine compositions range from Fo_{89}–Fo_{93}, but do not vary by more than 0.01 within single samples. CaO contents as high as 0.32 wt% are observed in some olivine grains, but most analyses range between 0.05 and 0.10 wt%.

Carbonates are less abundant in the lherzolites than in the pyroxenites (see following), and quantitative analyses were carried out in only

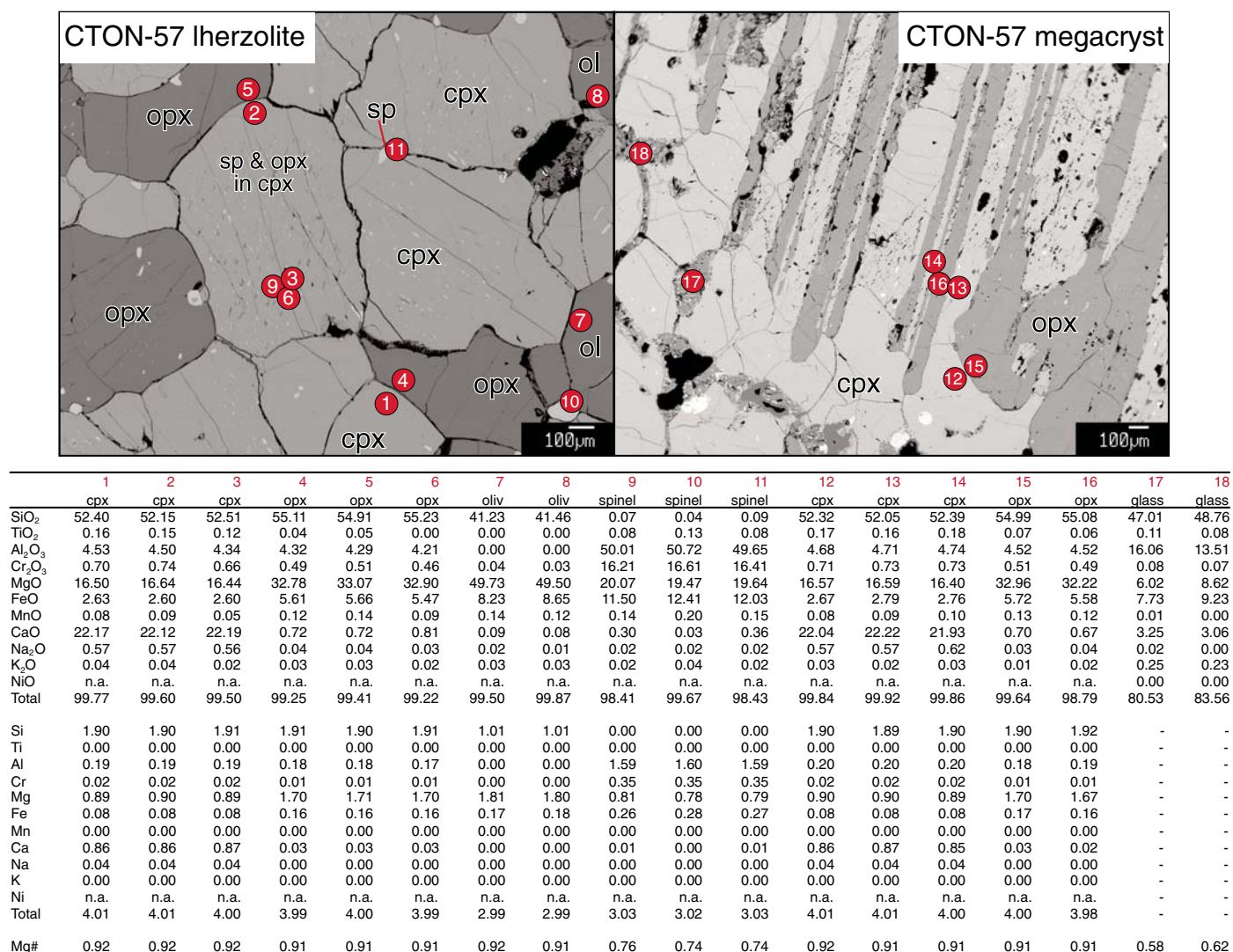|	1	2	3	4	5	6	7	8	9	10	11	12	13	14	15	16	17	18
	cpx	cpx	cpx	opx	opx	opx	oliv	oliv	spinel	spinel	spinel	cpx	cpx	cpx	opx	opx	glass	glass
SiO_2	52.40	52.15	52.51	55.11	54.91	55.23	41.23	41.46	0.07	0.04	0.09	52.32	52.05	52.39	54.99	55.08	47.01	48.76
TiO_2	0.16	0.15	0.12	0.04	0.05	0.00	0.00	0.00	0.08	0.13	0.08	0.17	0.16	0.18	0.07	0.06	0.11	0.02
Al_2O_3	4.53	4.50	4.34	4.32	4.29	4.21	0.00	0.00	50.01	50.72	49.65	4.68	4.71	4.74	4.52	4.52	16.06	13.51
Cr_2O_3	0.70	0.74	0.66	0.49	0.51	0.46	0.04	0.03	16.21	16.61	16.41	0.71	0.73	0.73	0.51	0.49	0.08	0.07
MgO	16.50	16.64	16.44	32.78	33.07	32.90	49.73	49.50	20.07	19.47	19.64	16.57	16.59	16.40	32.96	32.22	6.02	8.62
FeO	2.63	2.60	2.60	5.61	5.66	5.47	8.23	8.65	11.50	12.41	12.03	2.67	2.79	2.76	5.72	5.58	7.73	9.23
MnO	0.08	0.09	0.05	0.12	0.14	0.09	0.14	0.12	0.14	0.20	0.15	0.08	0.09	0.10	0.13	0.12	0.01	0.00
CaO	22.17	22.12	22.19	0.72	0.72	0.81	0.09	0.08	0.30	0.03	0.36	22.04	22.22	21.93	0.70	0.67	3.25	3.06
Na_2O	0.57	0.57	0.56	0.04	0.04	0.03	0.02	0.01	0.02	0.02	0.02	0.57	0.57	0.62	0.03	0.04	0.02	0.00
K_2O	0.04	0.04	0.02	0.03	0.03	0.02	0.03	0.03	0.02	0.04	0.02	0.03	0.02	0.03	0.01	0.02	0.25	0.23
NiO	n.a.	n.a.	n.a.	n.a.	n.a.	n.a.	n.a.	n.a.	n.a.	n.a.	n.a.	n.a.	n.a.	n.a.	n.a.	n.a.	0.00	0.00
Total	99.77	99.60	99.50	99.25	99.41	99.22	99.50	99.87	98.41	99.67	98.43	99.84	99.92	99.86	99.64	98.79	80.53	83.56
Si	1.90	1.90	1.91	1.91	1.90	1.91	1.01	1.01	0.00	0.00	0.00	1.90	1.89	1.90	1.90	1.92	-	-
Ti	0.00	0.00	0.00	0.00	0.00	0.00	0.00	0.00	0.00	0.00	0.00	0.00	0.00	0.00	0.00	0.00	-	-
Al	0.19	0.19	0.19	0.18	0.18	0.17	0.00	0.00	1.59	1.60	1.59	0.20	0.20	0.20	0.18	0.19	-	-
Cr	0.02	0.02	0.02	0.01	0.01	0.01	0.00	0.00	0.35	0.35	0.35	0.02	0.02	0.02	0.01	0.01	-	-
Mg	0.89	0.90	0.89	1.70	1.71	1.70	1.81	1.80	0.81	0.78	0.79	0.90	0.90	0.89	1.70	1.67	-	-
Fe	0.08	0.08	0.08	0.16	0.16	0.16	0.17	0.18	0.26	0.28	0.27	0.08	0.08	0.08	0.17	0.16	-	-
Mn	0.00	0.00	0.00	0.00	0.00	0.00	0.00	0.00	0.00	0.00	0.00	0.00	0.00	0.00	0.00	0.00	-	-
Ca	0.86	0.86	0.87	0.03	0.03	0.03	0.00	0.00	0.01	0.00	0.01	0.86	0.87	0.85	0.03	0.02	-	-
Na	0.04	0.04	0.04	0.00	0.00	0.00	0.00	0.00	0.00	0.00	0.00	0.04	0.04	0.04	0.00	0.00	-	-
K	0.00	0.00	0.00	0.00	0.00	0.00	0.00	0.00	0.00	0.00	0.00	0.00	0.00	0.00	0.00	0.00	-	-
Ni	n.a.	n.a.	n.a.	n.a.	n.a.	n.a.	n.a.	n.a.	n.a.	n.a.	n.a.	n.a.	n.a.	n.a.	n.a.	n.a.	-	-
Total	4.01	4.01	4.00	3.99	4.00	3.99	2.99	2.99	3.03	3.02	3.03	4.01	4.01	4.00	4.00	3.98	-	-
Mg#	0.92	0.92	0.92	0.91	0.91	0.91	0.92	0.91	0.76	0.74	0.74	0.92	0.91	0.91	0.91	0.91	0.58	0.62

Figure 4. Backscattered-electron (BSE) images of matrix and a pyroxene megacryst in lherzolite sample CTON-57. Numbers show locations of representative microprobe analyses listed in the table below. Abbreviations: opx—orthopyroxene, cpx—clinopyroxene, ol—olivine, sp—spinel.

a single lherzolite sample (CTON-53, Fig. 6). In this sample, calcite is intergrown with and appears to be replacing olivine in response to melt-rock interaction (Fig. 6). Some of the calcite grains in this sample show oscillatory growth zones with 0.0–1.0 wt% MnO.

Glass compositions were determined along grain boundaries and in discrete melt pockets associated with clinopyroxene, orthopyroxene ± calcite in samples CTON-57 and CTON-53. Most analyses have oxide totals in the 80–84 wt% range, consistent with large amounts of H_2O and/or CO_2 in the glass. The glasses have SiO_2 contents of 35–48 wt%, Al_2O_3 contents around 12%, and Mg numbers of ~60; all are strongly enstatite normative. The presence of calcite and pyroxene crystals in the melt pockets indicates that the glasses are not primary melt compositions.

Pyroxenites

We examined >70 pyroxenite xenoliths, which we subdivide here based on the presence or absence of garnet and the types of spinel and clinopyroxene present. In all of the pyroxenites, clinopyroxene is significantly more abundant than orthopyroxene, and olivine is rare to absent. Primary carbonate is present in many of the aluminous pyroxenites and a few of the Cr-diopside pyroxenites. All of the pyroxenites are characterized by irregular grain sizes and shapes and complex intergrowths between phases. In contrast to the lherzolites, however, there is little evidence of significant strain accumulation in any of the pyroxenites.

Cr-Diopside Pyroxenite

Cr-diopside pyroxenites are bright green in hand sample, contain abundant Cr-rich spinel, lack garnet, and are texturally well equilibrated (e.g., CTON-21 and CTON-67 in Fig. 3). A few of these samples contain up to 10% olivine, but most have little to no olivine. Many Cr-diopside pyroxenites contain euhedral orthopyroxene grains with finely exsolved cores and unexsolved rims; coarse exsolution and intergrowth textures in pyroxenes are rare. No crosscutting relationships are observed between Cr-diopside pyroxenites and either spinel lherzolites or other pyroxenite types. However, there is gradational layering between Cr-diopside pyroxenite and lherzolite in several samples.

Pyroxene and spinel compositions in the Cr-diopside pyroxenites (Figs. 5 and 7) are generally similar to those in the lherzolites and distinctly different from those in the garnet-spinel and spinel-absent pyroxenites. Clinopyroxene has 8%–11% jadeite component and orthopyroxene has ~4% Mg-Tschermak component. Spinel has Cr/Cr + Al ratios of 0.11–0.24 and Mg numbers of 70–75.

Spinel ± Garnet Pyroxenite and Spinel-Absent Pyroxenite

These pyroxenites are black in hand sample and are dominantly composed of clinopyroxene (up to 80 modal%). Many of the pyroxene grains show complex intergrowth relationships with one another. These intergrowths usually comprise two clinopyroxene grains, with less common clinopyroxene-orthopyroxene intergrowths. Many clinopyroxene grains contain rounded orthopyroxene inclusions (Fig. 8) that are in optical continuity with one another, suggesting replacement or overgrowth of original orthopyroxene by clinopyroxene. The garnet-bearing pyroxenites (e.g., CTON-17, CTON-77, and CTON-81 in Fig. 3) contain small (<0.5 mm) relict garnet grains and fragments that are surrounded by dark glassy to symplectitic rims that are similar to kelyphytic rims described by others in garnet pyroxenites and peridotites (e.g., Henjes-Kunst and Altherr, 1992; Stern et al., 1999; Sapienza et al., 2001). The garnet grains are always in close spatial association with large black spinel grains, although there is no clear textural evidence for a reaction relationship between the two phases (Figs. 9 and 10). Spinel is abundant in all of the garnet-bearing samples,
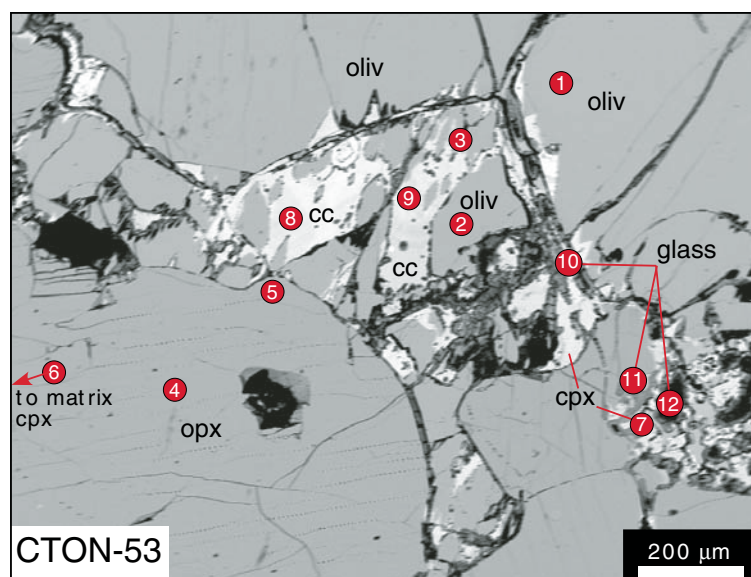
	1	2	3	4	5	6	7	8	9	10	11	12
	oliv	oliv	oliv	opx	opx	cpx	cpx	calcite	calcite	glass	glass	glass
SiO_2	41.09	41.10	41.12	55.70	55.78	52.71	53.07	0.00	0.20	47.39	45.00	56.12
TiO_2	0.00	0.00	0.00	0.01	0.00	0.04	0.07	0.03	0.06	0.13	0.10	0.18
Al_2O_3	0.01	0.01	0.01	3.42	3.52	3.75	5.35	0.08	0.16	13.26	13.96	20.58
Cr_2O_3	0.04	0.03	0.03	0.48	0.54	0.82	0.96	0.01	0.07	0.05	2.54	0.05
MgO	49.24	49.44	49.72	33.07	33.58	16.66	17.83	2.50	1.85	7.86	8.60	4.14
FeO	8.66	8.42	8.40	5.70	5.63	2.79	2.89	0.15	0.11	8.57	10.56	3.28
MnO	0.14	0.12	0.13	0.14	0.13	0.10	0.11	0.77	1.01	0.00	0.03	0.05
CaO	0.06	0.12	0.32	0.71	0.75	22.09	19.19	56.18	58.18	2.98	3.18	9.17
Na_2O	0.00	0.00	0.01	0.04	0.04	0.65	0.91	0.00	0.04	0.09	0.08	2.23
K_2O	0.02	0.02	0.03	0.03	0.03	0.03	0.01	0.02	0.02	0.18	0.24	0.33
Total	99.26	99.26	99.77	99.29	99.98	99.64	100.38	59.74	61.70	80.51	84.27	96.10
Si	1.01	1.01	1.00	1.93	1.92	1.92	1.90	0.00	0.00			
Ti	0.00	0.00	0.00	0.00	0.00	0.00	0.00	0.00	0.00			
Al	0.00	0.00	0.00	0.14	0.14	0.16	0.23	0.00	0.00			
Cr	0.00	0.00	0.00	0.01	0.01	0.02	0.03	0.00	0.00			
Mg	1.80	1.81	1.81	1.71	1.72	0.90	0.95	0.06	0.04			
Fe	0.18	0.17	0.17	0.17	0.16	0.09	0.09	0.00	0.00			
Mn	0.00	0.00	0.00	0.00	0.00	0.00	0.00	0.01	0.01			
Ca	0.00	0.00	0.01	0.03	0.03	0.86	0.74	0.93	0.93			
Na	0.00	0.00	0.00	0.00	0.00	0.05	0.06	0.00	0.00			
K	0.00	0.00	0.00	0.00	0.00	0.00	0.00	0.00	0.00			
Total	2.99	2.99	3.00	3.99	4.00	4.01	4.00	1.00	1.00			
Mg#	0.91	0.91	0.91	0.91	0.91	0.91	0.92	0.97	0.97	0.62	0.59	0.69

Figure 5. Backscattered-electron (BSE) image and microprobe analyses from carbonate-bearing lherzolite sample CTON-53. Abbreviations: opx—orthopyroxene, cpx—clinopyroxene, oliv—olivine, cc—calcite.
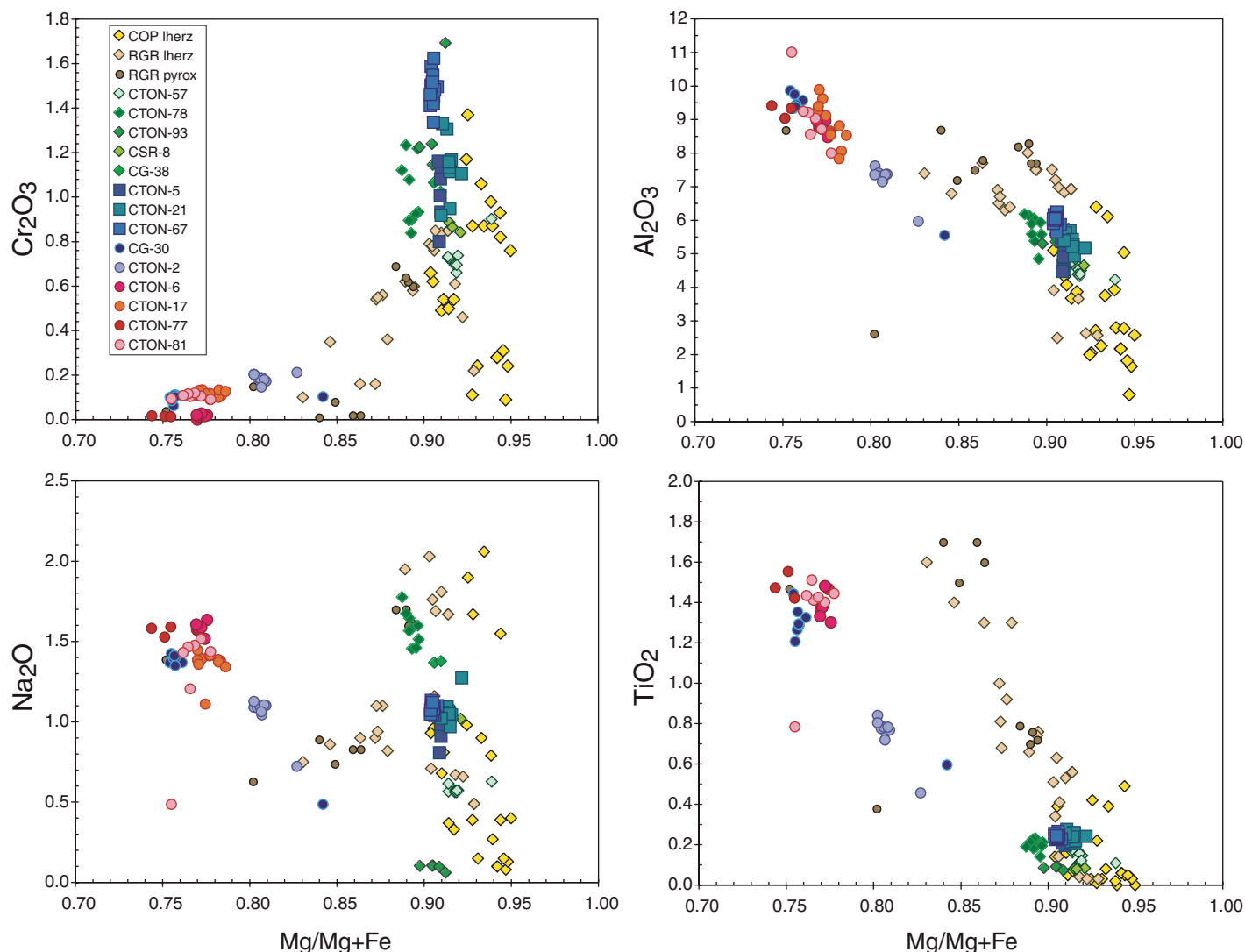
Figure 6. Clinopyroxene compositions as a function of host rock type. Diamonds—spinel lherzolites, squares—Cr-diopside pyroxenites, circles—spinel ± garnet pyroxenites; the four garnet-bearing samples are shown in reds and oranges. COP—Colorado Plateau lherzolites for comparison (data from Smith, 2000). RGR—Rio Grande rift lherzolites and pyroxenites for comparison (data from Baldridge, 1979; Wilshire et al., 1988; Smith, 2000).

typically as large (up to 3 mm) black grains. Small green spinel grains locally rim the black spinels, particularly in symplectites adjacent to garnet (Fig. 11). Reaction rims surrounding spinel are discussed in a subsequent section.

Fluid and glass inclusion trails are abundant throughout all pyroxenite samples; crosscutting relationships indicate that multiple generations are present and some trails contain both types of inclusions. Glass also occurs within symplectites around garnet and spinel and in melt pockets at grain triple junctions. The melt pockets typically contain carbonate in addition to silicate glass (see following). Olivine is rare to absent in the garnet pyroxenites, and it is confined to small inclusions within pyroxene. Rare phlogopite is present as inclusions in pyroxene grains.

Many pyroxenite samples that lack garnet are texturally akin to the garnet pyroxenites. These samples contain abundant large black spinels that are similar to those observed in association with garnet in the previously described samples. Pyroxenes in these samples show complex intergrowths and replacement textures that are also similar to those in the garnet pyroxenites. Based on these characteristics, it is likely that garnet was originally widespread in the pyroxenites beneath Cerrito Negro and other necks, but it reacted out of most samples prior to entrainment or during transport to the surface.

A few samples of pyroxenite (e.g., CTON-7 in Fig. 3) lack both spinel and garnet. These samples are otherwise similar to the garnet pyroxenites in that they contain large, irregular,

and interlocking pyroxene grains. Optically continuous inclusions of orthopyroxene within clinopyroxene are common. Both pyroxene types are exsolved on a variety of scales.

Pyroxene compositions within the spinel ± garnet and spinel-absent pyroxenites are much more aluminous than those in the Cr-diopside pyroxenites (Figs. 5 and 8–10). Clinopyroxene is augite with 14–16 mol% jadeite component; orthopyroxene is enstatite-rich with 7–11 mol% Mg-Tschermak component. Mg-numbers for both clinopyroxene and orthopyroxene range from 74 to 83, and garnet-bearing samples are the most Fe-enriched. Cr_2O_3 decreases and Al_2O_3, TiO_2, and Na_2O increase with decreasing Mg-number for both clinopyroxene (Fig. 5) and orthopyroxene. Cr_2O_3 is lower and Al_2O_3

338   Geosphere, December 2006

and TiO$_2$ are higher in the garnet-spinel and spinel-absent pyroxenites than in the Cr-spinel peridotites or lherzolites. CaO is higher in orthopyroxene and lower in clinopyroxene in all of the pyroxenites relative to the lherzolites, suggesting equilibration at higher temperatures (see following).

Relict garnet grains are present in pyroxenites CTON-6, CTON-17, CTON-77, and CTON-81 (Figs. 9 and 10). Garnet grains large enough to analyze have average compositions of Pyr$_{61}$Alm$_{26}$Grs$_{13}$Sps$_1$ and show a minor decrease in Mg (<5 mol %) and increase in Ca (2–5 mol %) in their glassy rim regions. Black spinels in the garnet pyroxenites are spinel-hercynite solid solutions with Mg numbers of 58–60. Cr$_2$O$_3$ contents are <0.3 wt% (Figs. 9 and 10). Green spinel grains in symplectites are very similar in composition to black spinel grains. Clinopyroxene compositions within the symplectites are nearly identical to matrix compositions, but orthopyroxene shows markedly lower Al$_2$O$_3$ (~6 versus 10 wt%) and higher SiO$_2$ (~52 versus 49 wt%) contents in the symplectites than in the matrix (e.g., see analyses in Fig. 10). Plagioclase was detected optically in symplectite rims around spinel and confirmed via quantitative electron microprobe analysis and X-ray maps. Due to the very small grain size in the symplectites, most analyses of plagioclase were mixed, but the few stoichiometric analyses that were obtained yielded compositions of An$_{93}$. Carbonates from Cerrito Negro are calcite with a minor dolomite component. Many samples show concentric Mn zoning that is similar to that observed in lherzolite sample CTON-53. A single sample from Cerro de Guadalupe (CG-40) contains oscillatory zoned dolomite.

Carbonate-Bearing Samples

Calcite occurs in many of the aluminous pyroxenites, including two of the garnet-bearing samples from this study, and in a few of the lherzolites. In general, xenoliths that contain abundant carbonate are the least well equilibrated texturally. Calcite grains as large as 2 mm occur at triple junctions between pyroxene grains, as inclusions in pyroxene (e.g., Fig. 12), within trails and clusters of melt inclusions, along grain boundaries, and within fractures. Many of the calcite grains contain concentric bands of glass inclusions and show oscillatory Mn zoning (Fig. 12; see also Figure 2d of Perkins et al., 2006). In almost every case, calcite is intergrown with or adjacent to orthopyroxene grains (Figs. 12 and 13). Clinopyroxene is typically strongly zoned toward lower Al, Ti, and Na contents adjacent to calcite (Fig. 13). Fluid/glass inclusion trails terminate at calcite grain boundaries and do not crosscut either the calcite
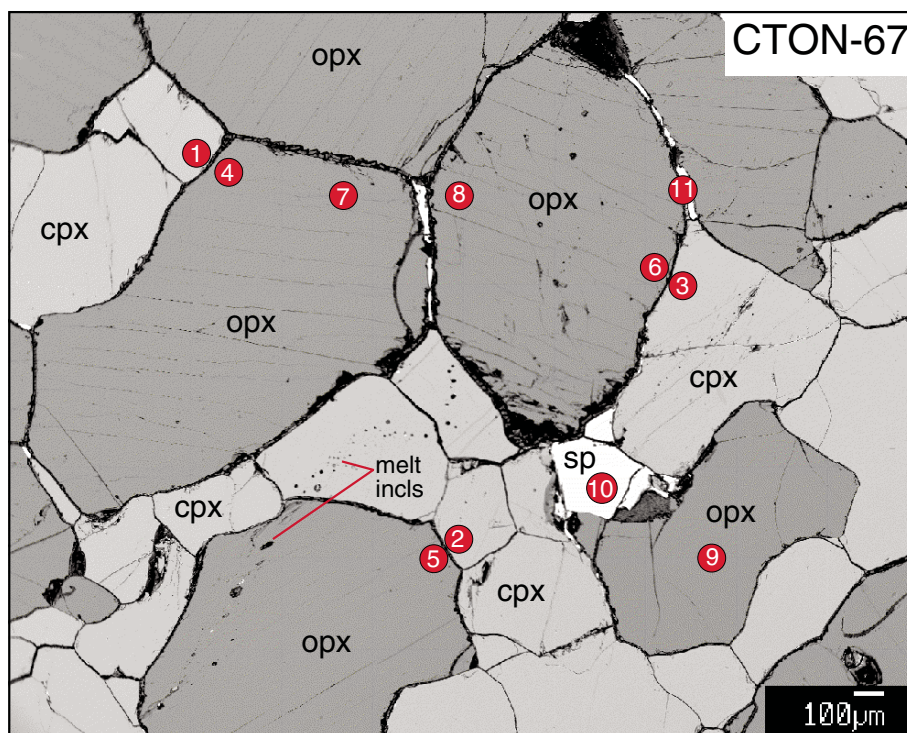
	1	2	3	4	5	6	7	8	9	10	11
	cpx	cpx	cpx	opx	opx	opx	opx	opx	opx	spinel	spinel
SiO$_2$	52.29	52.34	52.51	55.09	54.62	54.71	54.88	55.64	55.02	0.00	0.00
TiO$_2$	0.24	0.25	0.23	0.05	0.06	0.05	0.05	0.04	0.06	0.05	0.06
Al$_2$O$_3$	6.02	6.18	5.89	4.92	5.48	5.47	4.99	3.89	5.26	45.76	45.95
Cr$_2$O$_3$	1.50	1.59	1.50	0.86	0.93	0.86	0.89	0.58	0.79	22.33	22.05
MgO	14.99	14.73	15.02	31.49	31.25	31.15	31.45	32.02	31.23	17.32	17.39
FeO	2.84	2.79	2.73	7.35	7.38	7.21	7.40	7.44	7.42	13.97	13.98
MnO	0.10	0.15	0.13	0.18	0.20	0.17	0.19	0.17	0.18	0.20	0.21
CaO	21.34	21.40	21.44	0.54	0.52	0.55	0.56	0.55	0.52	0.00	0.02
Na$_2$O	1.11	1.14	1.10	0.05	0.03	0.04	0.05	0.03	0.03	n.a.	n.a.
K$_2$O	n.a.	n.a.	n.a.	n.a.	n.a.	n.a.	n.a.	n.a.	n.a.	n.a.	n.a.
NiO	0.09	0.08	0.11	0.11	0.13	0.11	0.10	0.11	0.11	0.31	0.27
Total	100.52	100.64	100.66	100.65	100.60	100.31	100.57	100.46	100.60	99.93	99.92
Si	1.89	1.89	1.89	1.90	1.89	1.89	1.90	1.92	1.90	0.00	0.00
Ti	0.01	0.01	0.01	0.00	0.00	0.00	0.00	0.00	0.00	0.00	0.00
Al	0.26	0.26	0.25	0.20	0.22	0.22	0.20	0.16	0.21	1.48	1.49
Cr	0.04	0.05	0.04	0.02	0.03	0.02	0.02	0.02	0.02	0.49	0.48
Mg	0.81	0.79	0.81	1.62	1.61	1.61	1.62	1.65	1.61	0.71	0.71
Fe	0.09	0.08	0.08	0.21	0.21	0.21	0.21	0.21	0.21	0.32	0.32
Mn	0.00	0.00	0.00	0.01	0.01	0.00	0.01	0.01	0.01	0.00	0.00
Ca	0.83	0.83	0.83	0.02	0.02	0.02	0.02	0.02	0.02	0.00	0.00
Na	0.08	0.08	0.08	0.00	0.00	0.00	0.00	0.00	0.00	n.a.	n.a.
K	n.a.	n.a.	n.a.	n.a.	n.a.	n.a.	n.a.	n.a.	n.a.	n.a.	n.a.
Ni	0.00	0.00	0.00	0.00	0.00	0.00	0.00	0.00	0.00	0.01	0.01
Total	3.99	3.99	3.99	3.99	3.99	3.98	3.99	3.99	3.98	3.01	3.01
Mg#	0.90	0.90	0.91	0.88	0.88	0.89	0.88	0.88	0.88	0.69	0.69

Figure 7. Backscattered-electron (BSE) image and microprobe analyses from Cr-diopside pyroxenite sample CTON-67. Abbreviations: opx—orthopyroxene, cpx—clinopyroxene, incls—inclusions, sp—spinel.

or the spatially associated orthopyroxene grains (Fig. 13). Oscillatory zoned dolomite is present in melt pockets in some xenoliths from Cerro de Guadalupe (see Figure 2g of Perkins et al., 2006) but was not observed in xenoliths from Cerrito Negro. Compositions of glass inclusions and glass pockets range from carbonatitic (SiO$_2$ = 1%–19%, oxide totals = 52%–75%) to silicate glasses similar to those in lherzolite CTON-53 described previously (e.g., Fig. 13).

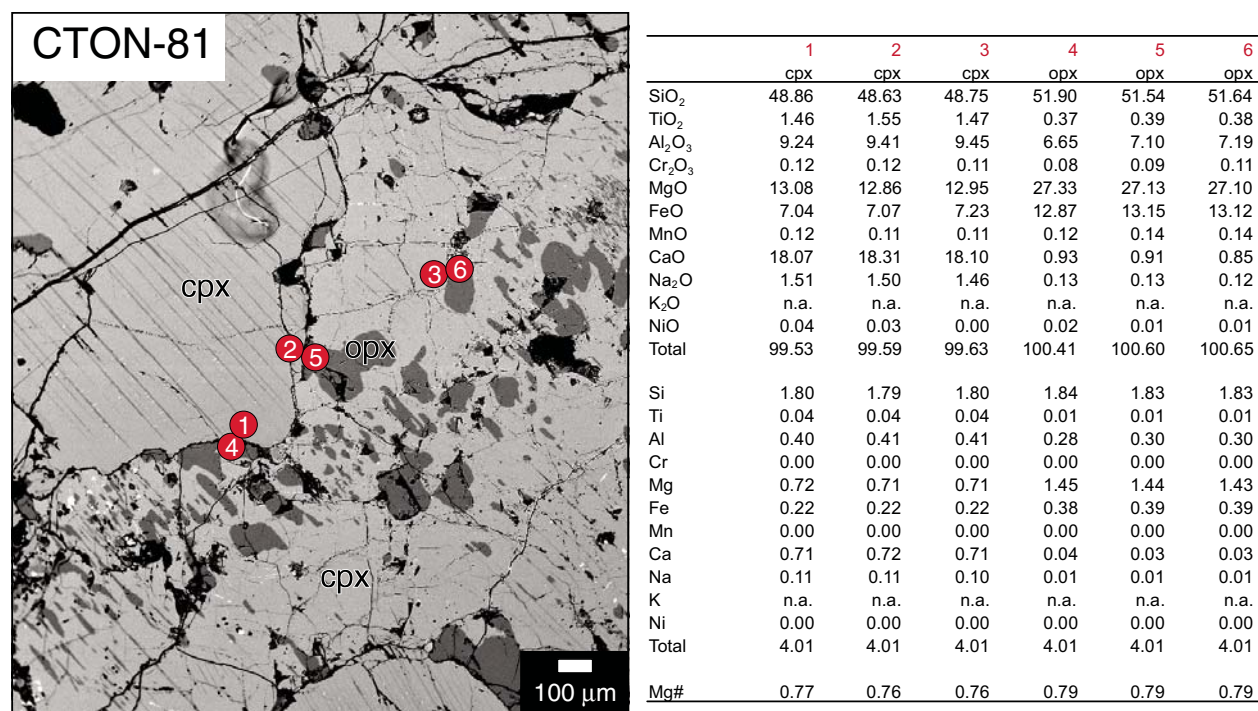|	1	2	3	4	5	6
	cpx	cpx	cpx	opx	opx	opx
SiO_2	48.86	48.63	48.75	51.90	51.54	51.64
TiO_2	1.46	1.55	1.47	0.37	0.39	0.38
Al_2O_3	9.24	9.41	9.45	6.65	7.10	7.19
Cr_2O_3	0.12	0.12	0.11	0.08	0.09	0.11
MgO	13.08	12.86	12.95	27.33	27.13	27.10
FeO	7.04	7.07	7.23	12.87	13.15	13.12
MnO	0.12	0.11	0.11	0.12	0.14	0.14
CaO	18.07	18.31	18.10	0.93	0.91	0.85
Na_2O	1.51	1.50	1.46	0.13	0.13	0.12
K_2O	n.a.	n.a.	n.a.	n.a.	n.a.	n.a.
NiO	0.04	0.03	0.00	0.02	0.01	0.01
Total	99.53	99.59	99.63	100.41	100.60	100.65
Si	1.80	1.79	1.80	1.84	1.83	1.83
Ti	0.04	0.04	0.04	0.01	0.01	0.01
Al	0.40	0.41	0.41	0.28	0.30	0.30
Cr	0.00	0.00	0.00	0.00	0.00	0.00
Mg	0.72	0.71	0.71	1.45	1.44	1.43
Fe	0.22	0.22	0.22	0.38	0.39	0.39
Mn	0.00	0.00	0.00	0.00	0.00	0.00
Ca	0.71	0.72	0.71	0.04	0.03	0.03
Na	0.11	0.11	0.10	0.01	0.01	0.01
K	n.a.	n.a.	n.a.	n.a.	n.a.	n.a.
Ni	0.00	0.00	0.00	0.00	0.00	0.00
Total	4.01	4.01	4.01	4.01	4.01	4.01
Mg#	0.77	0.76	0.76	0.79	0.79	0.79

Figure 8. Backscattered-electron (BSE) image and microprobe analyses from intergrown pyroxenes in garnet pyroxenite sample CTON-81. Abbreviations: opx—orthopyroxene, cpx—clinopyroxene.

THERMOBAROMETRY

Temperatures for lherzolites and pyroxenites and pressures for garnet-bearing pyroxenites were calculated using the two-pyroxene thermometer and the Al-in-orthopyroxene barometer of Brey and Köhler (1990). Representative calculated temperatures are given for each rock type in Table 1. In lherzolites, compositions were selected from adjacent clinopyroxene and orthopyroxene grains with well-equilibrated textures, as well as from adjacent lamellae in locally present, coarsely exsolved megacrysts (e.g., Fig. 4). The general scarcity of orthopyroxene in some of the pyroxenites resulted in selection of both adjacent and nonadjacent mineral pairs. Temperature calculations for pyroxenites based on nonadjacent pyroxenes yield temperatures ~30 °C lower than those from adjacent pyroxene grains. Compositional data for garnet-orthopyroxene pressure calculations were chosen based on the presence of garnets large enough for microprobe analysis that were also near orthopyroxene grains. Coherent garnet grains juxtaposed immediately against adjacent orthopyroxene are rare due to the large symplectite rims around most garnet grains, but orthopyroxene is generally abundant immediately surrounding the symplectites.

Temperatures for the lherzolites range from 900 to 1000 °C at a reference pressure of 15 kbar

(Fig. 14). The presence of coarsely exsolved megacrysts in some of the lherzolites hints at a higher-temperature history prior to the most recent episode of equilibration. Temperatures are generally higher for the pyroxenites than for the lherzolites, and they also show a broader range, from 950 to 1145 °C (Fig. 14A). Cr-spinel pyroxenites overlap the high-temperature end of the lherzolite range, garnet pyroxenites record temperatures from 1000 to 1145 °C, and carbonate-bearing pyroxenites (all types) record the highest temperatures.

Two of the garnet-bearing pyroxenite samples (CTON-6, CTON-77) record pressures of 16–18 kbar, whereas samples CTON-17 and CTON-81 record pressures of 11–14 kbar. The Brey and Köhler (1990) geobarometer is extremely sensitive to calculated ferric iron content in garnet. Garnets in CTON-6 and CTON-77 have calculated Fe^{3+} of 0.048–0.060 cations per formula unit (p.f.u.), compared to $Fe^{3+} = 0$ in CTON-17 and CTON-81. Zero values for Fe^{3+} yield the lowest pressure estimates and are therefore assumed to provide only minimum constraints on pressures experienced by the samples. Pressures in all samples must have been greater than 11 kbar, which corresponds to the inferred depth to the Moho beneath the Puerco necks (West et al., 2004). The samples that record higher pressures have narrower symplectites around garnet than the

samples that record lower pressures. We thus take the 16–18 kbar values as more realistic for garnet growth and initial equilibration (Fig. 14) and interpret the lower pressures to represent reequilibration during decompression.

WHOLE-ROCK COMPOSITIONS

Whole-rock major-element data were obtained for 10 spinel ± garnet pyroxenites and 11 lherzolites by X-ray fluorescence (XRF) of fused disks using the Rigaku RIX 2100 at the University of New Mexico (Table 2). None of the Cr-diopside pyroxenites was analyzed as part of this study. Most samples were titrated to determine concentrations of FeO and Fe_2O_3. Whole-rock data for the host basalts were taken from Hallett (1994). None of the Cr-diopside pyroxenite xenoliths was large enough to crush for whole-rock analysis.

The CaO/Al_2O_3 ratios range from 0.66 to 1.44 in the lherzolites, and from 0.34 to 2.09 in the pyroxenites. Mg-numbers are 90–91 in the lherzolites, but scatter between 72 and 82 in the pyroxenites. Most of the pyroxenites are enstatite-normative and are chemically similar to Wilshire et al.'s (1988) Cr-diopside websterite analyses, despite the low Cr content of their pyroxenes; three pyroxenites are nepheline-normative and are similar to Wilshire et al.'s (1988) Al-augite clinopyroxenite samples.

Major-element data for the lherzolites, spinel ± garnet pyroxenites, and basalts, and microprobe analyses of silicate and carbonate melt inclusions are plotted against MgO in Figure 15. For all oxides except SiO_2, the pyroxenites plot within a triangle defined by lherzolite, average Rio Puerco basalt, and the most Ca-rich carbonate melt inclusion composition.

ORIGIN OF PYROXENITES

Any model for the origin of the Rio Puerco pyroxenites has to take into account whole-rock chemical data, mineral compositions, temperatures of equilibration, and field and barometric evidence for formation in the spinel lherzolite facies in the mantle.

Clinopyroxenes from the Cr-diopside pyroxenites are similar to those from lherzolite xenoliths and are characterized by high Cr_2O_3 and Mg/Mg + Fe, low TiO_2, and moderate Al_2O_3 and Na_2O contents (Fig. 5). These characteristics are consistent with formation of the Cr-diopside pyroxenites via removal of an alkali basaltic melt component from a lherzolitic precursor (Hart and Dunn, 1993).

As shown in Figure 15, the spinel ± garnet pyroxenites differ significantly in major-element composition from the erupted alkali basalts from the Rio Puerco necks (basalt data from Hallett, 1994) and from the silicate melt inclusion compositions. The pyroxenites show some similarities to picrite compositions from the GEOROC database (http://georoc.mpch-maintz.gwdg.de/georoc/Entry.html), but generally have higher CaO and MgO contents and lower Na_2O and Al_2O_3 contents than picrites. Based on these data, it is unlikely that the pyroxenites represent primary melt compositions. The complex intergrowth textures preserved in most of the spinel ± garnet pyroxenites, coupled with localized pyroxenite development in crosscutting veins/dikes, are inconsistent with a crystal settling origin for the pyroxenites, although cumulate-like compositions could result from melt crystallization on conduit walls (e.g., Irving, 1980). Fractional removal of olivine and/or clinopyroxene from an alkali basalt would produce a remaining melt fraction that would be depleted in MgO and enriched in FeO, TiO_2, Al_2O_3, and Na_2O relative to the pyroxenites shown in Figure 15, and hence it also fails as a mechanism for pyroxenite formation.

Textural and chemical data from this study support the hypothesis of infiltration and addition of melt(s) to mantle lherzolite as an origin for Rio Puerco spinel ± garnet pyroxenites. In general, infiltration of silicic melt alone will favor conversion of olivine to orthopyroxene (e.g., Rapp et al., 1999; Prouteau et al., 2001;
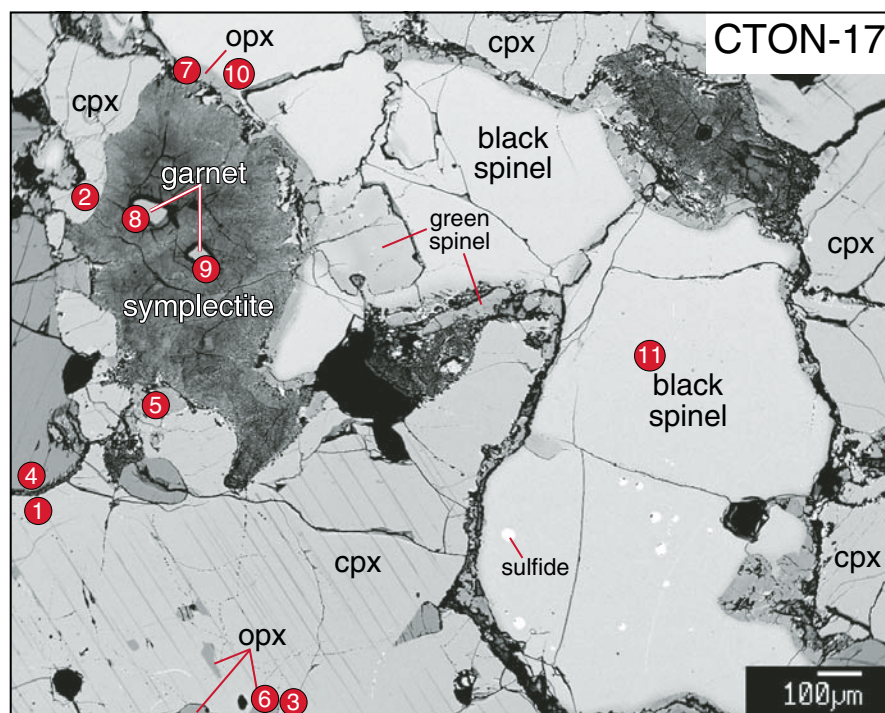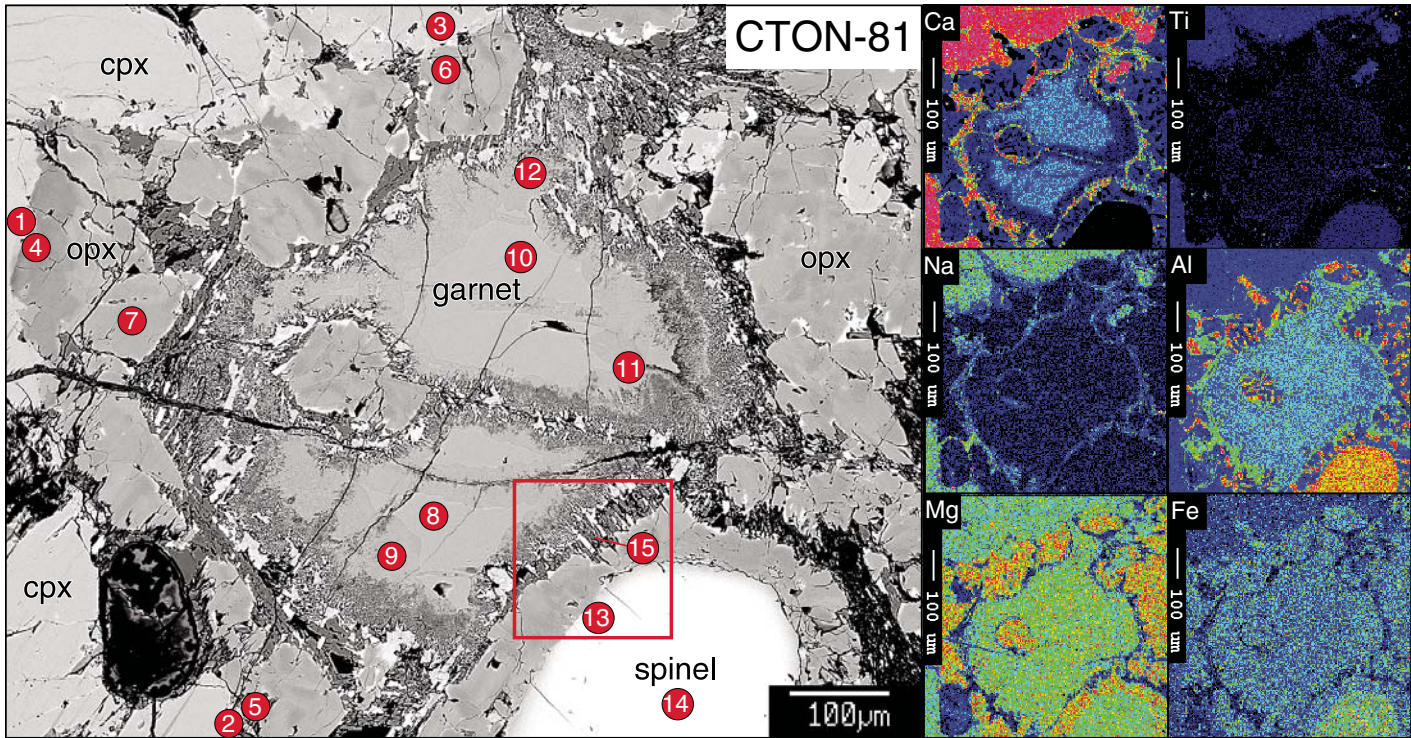

	1	2	3	4	5	6	7	8	9	10	11
	cpx	cpx	cpx	opx	opx	opx	opx	garnet	garnet	spinel	spinel
SiO_2	49.53	49.38	48.81	52.46	50.97	51.35	47.80	40.77	40.70	0.02	0.04
TiO_2	1.31	1.36	1.27	0.40	0.14	0.35	0.28	0.33	0.34	0.35	0.36
Al_2O_3	8.83	8.55	9.91	6.99	9.31	8.27	13.21	23.06	22.94	60.49	60.56
Cr_2O_3	0.14	0.13	0.13	0.12	0.11	0.12	0.11	0.12	0.08	0.09	0.09
MgO	13.54	13.61	13.11	27.30	24.43	26.51	23.66	16.94	16.83	17.95	17.70
FeO	6.73	6.62	6.97	12.21	12.72	12.51	12.26	12.73	12.71	21.51	21.77
MnO	0.11	0.14	0.12	0.17	0.47	0.20	0.39	0.37	0.37	0.09	0.09
CaO	18.80	19.05	18.59	1.08	1.68	0.96	1.59	5.74	5.57	n.a.	n.a.
Na_2O	1.38	1.35	1.36	0.12	0.02	0.12	0.06	n.a.	n.a.	n.a.	n.a.
NiO	0.04	0.01	0.02	0.02	0.03	0.03	0.00	n.a.	n.a.	0.18	0.18
V_2O_3	n.a.	n.a.	n.a.	n.a.	n.a.	n.a.	n.a.	n.a.	n.a.	0.18	0.16
Total	100.41	100.18	100.29	100.88	99.88	100.41	99.34	100.04	99.53	100.86	100.94
Si	1.81	1.81	1.79	1.85	1.82	1.82	1.72	2.96	2.97	0.00	0.00
Ti	0.04	0.04	0.03	0.01	0.00	0.01	0.01	1.97	1.97	0.01	0.01
Al	0.38	0.37	0.43	0.29	0.39	0.35	0.56	0.02	0.02	1.87	1.87
Cr	0.00	0.00	0.00	0.00	0.00	0.00	0.00	0.01	0.00	0.00	0.00
Mg	0.74	0.74	0.72	1.43	1.30	1.40	1.27	1.83	1.83	0.70	0.69
Fe	0.21	0.20	0.21	0.36	0.38	0.37	0.37	0.77	0.77	0.47	0.48
Mn	0.00	0.00	0.00	0.01	0.01	0.01	0.01	0.02	0.02	0.00	0.00
Ca	0.74	0.75	0.73	0.04	0.06	0.04	0.06	0.45	0.44	n.a.	n.a.
Na	0.10	0.10	0.10	0.01	0.00	0.01	0.00	n.a.	n.a.	n.a.	n.a.
Ni	0.00	0.00	0.00	0.00	0.00	0.00	0.00	n.a.	n.a.	0.00	0.00
V	n.a.	n.a.	n.a.	n.a.	n.a.	n.a.	n.a.	n.a.	n.a.	0.00	0.00
Total	4.01	4.01	4.01	4.00	3.98	4.00	4.00	8.03	8.03	3.06	3.06
Mg#	0.78	0.79	0.77	0.80	0.77	0.79	0.77	0.70	0.70	0.60	0.59

Figure 9. Backscattered-electron (BSE) image and microprobe analyses from garnet pyroxenite sample CTON-17, showing relict garnet surrounded by wide symplectic reaction zone. Abbreviations: opx—orthopyroxene, cpx—clinopyroxene.

Liu et al., 2005). The preferential development of clinopyroxene rather than orthopyroxene in the pyroxenites, however, requires infiltration of a melt with high Ca content and relatively low Si activity. The presence of both silicate and carbonatite melt inclusions within single xenolith samples implies infiltration of either a miscible carbonosilicate melt that subsequently unmixed, or lherzolite interaction with at least two infiltrating melts of widely varying composition.

As is evident from Figure 15, the pyroxenites could not have been produced via reaction of lherzolite with basaltic melt alone, but could represent mixtures that also involved a carbonatitic melt component. Calculations using basaltic melt with 8% MgO (Negro1 from Hallett, 1994), the most calcic carbonate melt inclusion from this study (from sample CG-40), and average lherzolite from this study were carried out in order to test the hypothesis

	1	2	3	4	5	6	7	8	9	10	11	12	13	14	15
	cpx	cpx	cpx	opx	opx	opx	opx	gar	gar	"gar"	"gar"	"gar"	spinel	spinel	plag
SiO_2	49.31	49.11	49.23	49.47	49.12	51.97	52.47	41.65	41.47	41.75	42.65	41.33	0.04	0.02	45.16
TiO_2	1.48	1.44	1.43	0.26	0.24	0.14	0.36	0.44	0.43	0.33	0.38	0.40	0.35	0.31	0.01
Al_2O_3	8.18	8.75	8.90	10.88	10.51	6.55	5.40	23.46	23.23	23.44	23.46	22.74	60.76	62.18	34.82
Cr_2O_3	0.10	0.11	0.11	0.09	0.09	0.08	0.08	0.11	0.11	0.09	0.09	0.10	0.11	0.08	0.02
MgO	13.42	13.81	13.46	25.41	23.44	25.26	27.75	16.76	16.66	16.87	16.64	17.73	18.36	16.97	0.18
FeO	6.86	7.55	7.10	11.87	13.67	13.88	12.47	13.62	13.34	13.56	13.25	14.08	21.53	21.30	0.89
MnO	0.12	0.13	0.10	0.25	0.41	0.43	0.12	0.40	0.36	0.39	0.40	0.43	0.12	0.16	0.02
CaO	18.36	17.62	17.79	1.73	2.50	1.88	0.90	5.31	5.17	5.36	5.15	4.77	n.a.	n.a.	18.62
Na_2O	1.47	1.23	1.55	0.05	0.02	0.00	0.11	n.a.	n.a.	n.a.	n.a.	n.a.	n.a.	n.a.	0.68
K_2O	n.a.	n.a.	n.a.	n.a.	n.a.	n.a.	n.a.	n.a.	n.a.	n.a.	n.a.	n.a.	n.a.	n.a.	0.00
NiO	0.01	0.04	0.03	0.00	0.03	0.00	0.04	n.a.	n.a.	n.a.	n.a.	n.a.	0.17	0.20	n.a.
Total	99.30	99.79	99.72	100.01	100.01	100.19	99.73	101.74	100.76	101.79	102.01	101.58	101.43	101.20	100.39
Si	1.82	1.81	1.81	1.76	1.77	1.86	1.87	2.98	2.99	2.98	3.03	2.97	0.00	0.00	2.07
Ti	0.04	0.04	0.04	0.01	0.01	0.00	0.01	0.02	0.02	0.02	0.02	0.02	0.01	0.01	0.00
Al	0.36	0.38	0.39	0.46	0.45	0.28	0.23	1.98	1.97	1.97	1.96	1.92	1.86	1.90	1.89
Cr	0.00	0.00	0.00	0.00	0.00	0.00	0.00	0.01	0.01	0.01	0.01	0.01	0.00	0.00	0.00
Mg	0.74	0.76	0.74	1.35	1.26	1.35	1.48	1.78	1.79	1.80	1.76	1.90	0.71	0.66	0.01
Fe	0.21	0.23	0.22	0.35	0.41	0.42	0.37	0.81	0.80	0.81	0.79	0.85	0.47	0.46	0.03
Mn	0.00	0.00	0.00	0.01	0.01	0.01	0.00	0.02	0.02	0.02	0.02	0.03	0.00	0.00	0.00
Ca	0.73	0.69	0.70	0.07	0.10	0.07	0.03	0.41	0.40	0.41	0.39	0.37	n.a.	n.a.	0.92
Na	0.11	0.09	0.11	0.00	0.00	0.00	0.01	n.a.	n.a.	n.a.	n.a.	n.a.	n.a.	n.a.	0.06
K	n.a.	n.a.	n.a.	n.a.	n.a.	n.a.	n.a.	n.a.	n.a.	n.a.	n.a.	n.a.	n.a.	n.a.	0.00
Ni	0.00	0.00	0.00	0.00	0.00	0.00	0.00	n.a.	n.a.	n.a.	n.a.	n.a.	0.00	0.00	0
Total	4.01	4.01	4.01	4.00	4.00	3.99	4.01	8.01	8.00	8.01	7.97	8.05	3.06	3.04	4.99
Mg#	0.78	0.77	0.77	0.79	0.75	0.76	0.80	0.69	0.69	0.69	0.69	0.69	0.60	0.59	

Figure 10. Backscattered-electron (BSE) image, X-ray element maps, and microprobe analyses from garnet reaction zone in sample CTON-81. Red box indicates location of Figure 11. Abbreviations: opx—orthopyroxene, cpx—clinopyroxene, gar—garnet, plag—plagioclase.
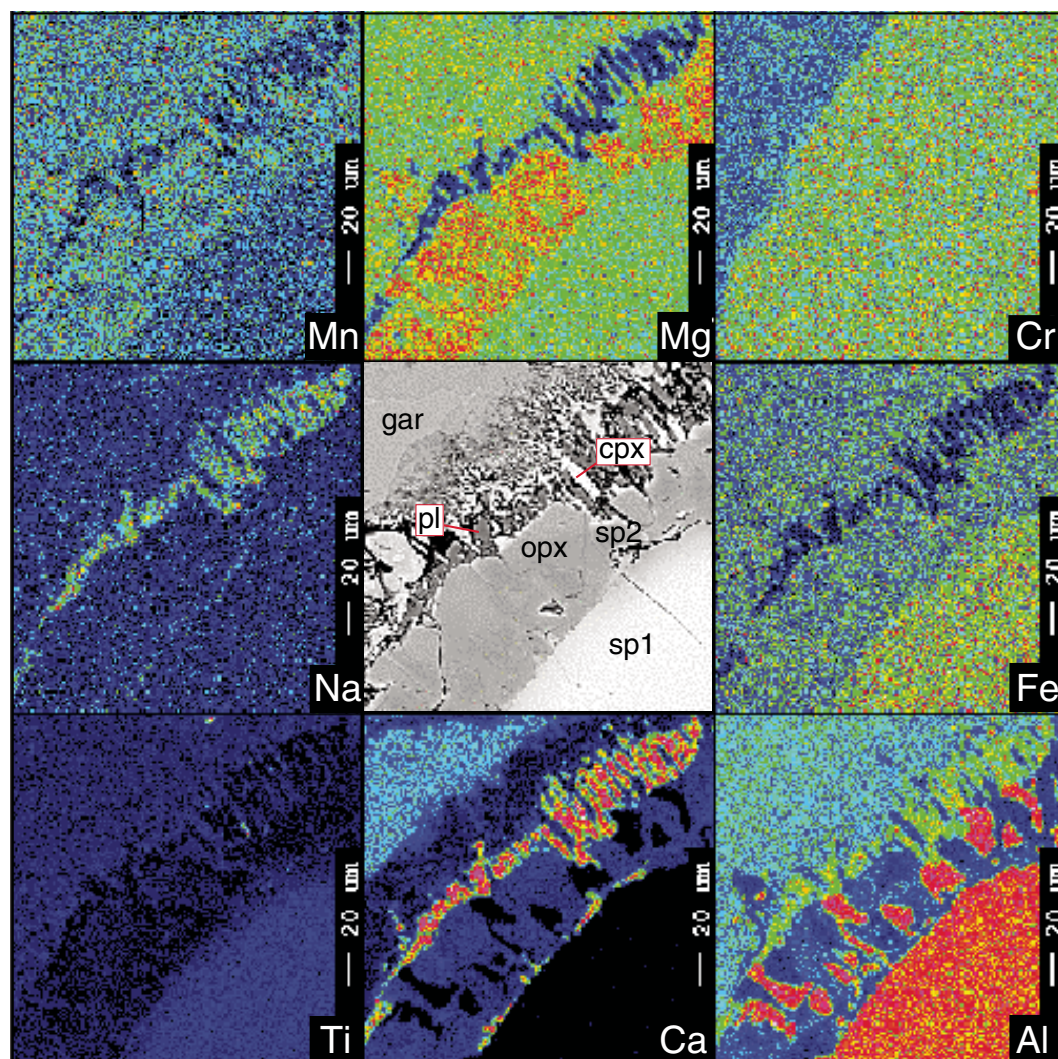
Figure 11. Detailed X-ray element maps of interface between garnet reaction zone and spinel reaction zone in sample CTON-81. Abbreviations: opx—orthopyroxene, cpx—clinopyroxene, gar—garnet, pl—plagioclase, sp—spinel.

that the pyroxenites formed via bulk mixing of lherzolite with silicate + carbonate melt. Al_2O_3, FeO_T, MgO, CaO, and MnO contents of the pyroxenites can be adequately matched via bulk mixing in the approximate proportions lherzolite$_{30-35}$-basalt$_{40-50}$-carbonatite$_{15-25}$ (e.g., Fig. 15). TiO_2 and Na_2O values of the pyroxenites can also be matched via mixing of ~35% lherzolite and 65% melt, but require a greater contribution from carbonatite relative to basaltic melt. The high SiO_2 content of the pyroxenites is not easily accounted for by any simple mixture of lherzolite + basalt + carbonatite, however. The Si values are similar to SiO_2 contents of clinopyroxene and orthopyroxene and likely reflect preferential consumption of olivine and formation of pyroxenes during lherzolite-melt interaction. Interestingly, the SiO_2 values are also consistent with mixing in the approximate proportions lherzolite$_{35}$melt$_{65}$.

Clinopyroxenes in the spinel ± garnet pyroxenites have very low Cr_2O_3 and Mg/Mg + Fe, and high Na_2O, TiO_2, and Al_2O_3 contents. These compositions are consistent with pyroxene growth in response to addition of melt to a lherzolitic precursor. The high Fe, Al, Ti, and Na contents are generally more consistent with infiltration of a silicate than a carbonatitic melt (Rudnick et al., 1993), but zoning toward lower Fe, Al, Ti, and Na adjacent to calcite inclusions and melt pockets (e.g., Fig. 13) clearly points toward involvement of a carbonatitic melt as well.

Thermobarometric data from the Rio Puerco xenoliths also support spinel pyroxenite formation in response to lherzolite-melt interaction if the lherzolites and pyroxenites were sampled from similar depths. These pyroxenites record temperatures that are as much as 200 °C hotter than lherzolites from the same necks (Fig. 14) and plot close to the pyroxenite solidus experimentally determined by Pertermann and Hirschmann (2003). Temperatures obtained from pyroxenes adjacent to melt pockets in spinel lherzolite samples are also ~200 °C hotter than the equilibrium

lherzolite values (Table 1). Geobarometry is consistent with pyroxenite equilibration at depths within the spinel lherzolite stability field. The high temperatures at these depths can most readily be reconciled with pyroxenite formation at melt conduit walls that crosscut spinel lherzolites (Fig. 16). The relatively similar calculated lherzolite:melt ratios needed to produce the analyzed pyroxenites suggest that reactive melt infiltration may have ceased once all olivine was consumed near the melt conduits. The large size (up to 30 cm in diameter) of many of the pyroxenite xenoliths indicates that melt was able to penetrate significant distances into the surrounding lherzolite during its ascent.
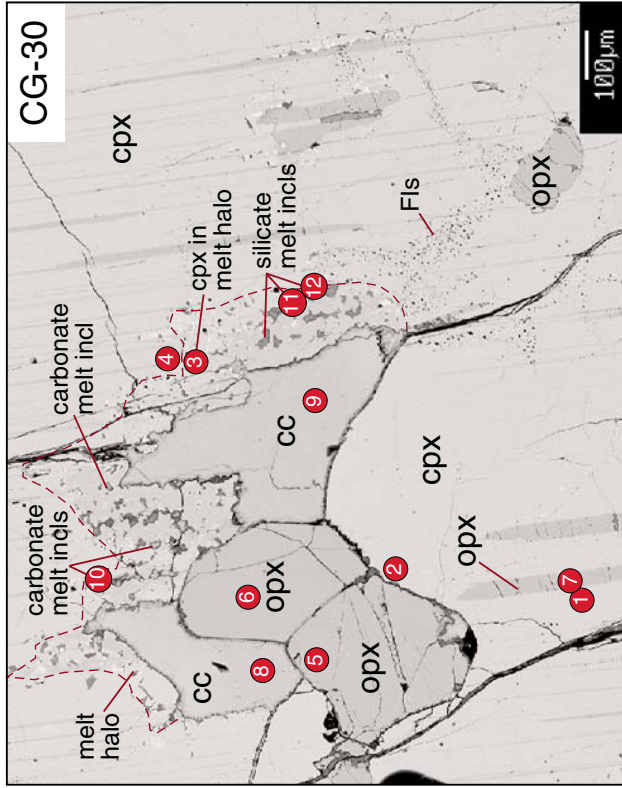
SPINEL ± GARNET PYROXENITE REACTION HISTORY

Textural evidence for two separate reactions involving garnet, spinel, and melt is seen in the spinel ± garnet pyroxenites. These reactions

Figure 13. Backscattered-electron (BSE) image and microprobe analyses from spinel pyroxenite sample CG-30. Calcite is intimately associated with orthopyroxene and surrounded by clinopyroxene. Both silicate and carbonate glass inclusions surround the calcite + orthopyroxene, and clinopyroxene is zoned toward lower Al, Ti, and Na contents in association with melt inclusions. Abbreviations: opx—orthopyroxene, cpx—clinopyroxene, incls—inclusions, cc—calcite, FIs—fluid inclusions.

	1 cpx	2 cpx	3 cpx	4 cpx	5 opx	6 opx	7 opx	8 calcite	9 calcite	10 carb melt	11 silicate melt	12 silicate melt
SiO_2	48.72	48.52	51.51	48.62	50.99	50.86	51.03	0.00	0.00	19.72	42.77	42.67
TiO_2	1.29	1.36	0.60	1.30	0.33	0.34	0.33	0.00	0.00	0.44	0.17	0.11
Al_2O_3	9.47	9.76	5.57	9.40	7.79	7.75	7.64	0.07	0.06	2.43	7.90	9.21
Cr_2O_3	0.11	0.11	0.11	0.11	0.08	0.07	0.07	0.07	0.06	0.09	0.05	0.07
MgO	13.20	13.00	17.59	13.10	26.49	26.61	26.71	4.40	3.82	7.46	18.15	19.19
FeO	7.54	7.46	5.90	7.50	14.34	14.47	14.22	4.23	3.68	9.84	13.71	14.93
MnO	0.17	0.14	0.14	0.16	0.20	0.19	0.22	0.37	0.36	0.88	0.04	0.04
CaO	18.92	19.03	18.87	19.31	0.95	0.96	0.89	54.39	51.52	32.02	3.84	2.75
Na_2O	1.40	1.41	0.49	1.35	0.12	0.10	0.09	0.05	0.05	0.16	0.04	0.03
K_2O	0.03	0.03	0.03	0.00	0.01	0.03	0.01	0.02	0.02	0.09	0.18	0.17
Total	100.85	100.83	100.80	100.85	101.30	101.37	101.20	63.53	59.50	73.15	86.86	89.17
Si	1.77	1.77	1.85	1.77	1.80	1.80	1.80	0.00	0.00	1.19	1.79	1.74
Ti	0.04	0.04	0.02	0.04	0.01	0.01	0.01	0.00	0.00	0.02	0.01	0.00
Al	0.41	0.42	0.24	0.40	0.32	0.32	0.32	0.00	0.00	0.17	0.39	0.44
Cr	0.00	0.00	0.00	0.00	0.00	0.00	0.00	0.00	0.00	0.00	0.00	0.00
Mg	0.72	0.71	0.94	0.71	1.39	1.40	1.41	0.09	0.09	0.67	1.13	1.17
Fe	0.23	0.23	0.18	0.23	0.42	0.43	0.42	0.05	0.05	0.50	0.48	0.51
Mn	0.01	0.00	0.00	0.00	0.01	0.01	0.01	0.01	0.00	0.05	0.00	0.00
Ca	0.74	0.74	0.73	0.75	0.04	0.04	0.03	0.84	0.85	2.07	0.17	0.12
Na	0.10	0.10	0.03	0.10	0.01	0.01	0.01	0.00	0.00	0.02	0.00	0.00
K	0.00	0.00	0.00	0.00	0.00	0.01	0.01	0.00	0.00	0.01	0.01	0.01
Total	4.01	4.01	4.00	4.01	4.00	4.01	4.00	1.00	1.00	4.69	3.99	4.01
Mg#	0.76	0.76	0.84	0.76	0.77	0.77	0.77	0.65	0.65	0.57	0.70	0.70

Figure 12. Backscattered-electron (BSE) image and microprobe analyses from carbonate-bearing, spinel-absent pyroxenite CTON-7. Note inclusions of orthopyroxene within calcite, which is itself included within clinopyroxene. Also note Mn zoning in calcite. Abbreviations: opx—orthopyroxene, cpx—clinopyroxene.

	1 calcite	2 calcite	3 calcite	4 calcite	5 calcite	6 cpx	7 cpx	8 cpx	9 opx	10 opx
SiO_2	n.a.	n.a.	n.a.	n.a.	n.a.	49.43	50.22	49.32	52.51	52.12
TiO_2	n.a.	n.a.	n.a.	n.a.	n.a.	0.81	0.81	0.75	0.26	0.26
Al_2O_3	n.a.	n.a.	n.a.	n.a.	n.a.	7.57	7.67	7.55	6.03	6.03
Cr_2O_3	n.a.	n.a.	n.a.	n.a.	n.a.	0.24	0.22	0.23	0.19	0.21
MgO	0.67	0.84	0.96	1.77	0.98	15.38	15.24	14.91	28.41	27.97
FeO	0.08	0.14	0.16	0.07	0.08	6.10	6.20	6.40	11.26	11.48
MnO	0.00	0.02	2.60	0.01	3.35	0.14	0.14	0.15	0.19	0.18
CaO	55.88	52.82	56.67	54.54	55.48	18.92	18.97	18.55	1.26	1.28
Na_2O	n.a.	n.a.	n.a.	n.a.	n.a.	1.22	1.21	1.25	0.13	0.10
NiO	0.00	0.00	0.00	0.00	0.00	0.01	0.03	0.01	0.11	0.10
SrO	0.00	0.00	0.00	0.00	0.17	n.a.	n.a.	n.a.	n.a.	n.a.
BaO	0.02	0.00	0.03	0.00	0.02	n.a.	n.a.	n.a.	n.a.	n.a.
Total	56.65	53.82	60.41	56.39	60.09	99.83	100.70	99.13	100.35	99.75
Si	n.a.	n.a.	n.a.	n.a.	n.a.	1.80	1.81	1.81	1.86	1.86
Ti	n.a.	n.a.	n.a.	n.a.	n.a.	0.02	0.02	0.02	0.01	0.01
Al	n.a.	n.a.	n.a.	n.a.	n.a.	0.32	0.33	0.33	0.25	0.25
Cr	n.a.	n.a.	n.a.	n.a.	n.a.	0.01	0.01	0.01	0.01	0.01
Mg	0.02	0.02	0.02	0.04	0.02	0.83	0.82	0.81	1.50	1.48
Fe	0.00	0.00	0.00	0.00	0.00	0.19	0.19	0.20	0.33	0.34
Mn	0.00	0.00	0.03	0.00	0.04	0.00	0.00	0.00	0.01	0.01
Ca	0.98	0.98	0.94	0.96	0.93	0.74	0.73	0.73	0.05	0.05
Na	n.a.	n.a.	n.a.	n.a.	n.a.	0.09	0.08	0.09	0.01	0.01
Ni	0.00	0.00	0.00	0.00	0.00	0.00	0.00	0.00	0.00	0.00
Sr	0.00	0.00	0.00	0.00	0.00	n.a.	n.a.	n.a.	n.a.	n.a.
Ba	0.00	0.00	0.00	0.00	0.00	n.a.	n.a.	n.a.	n.a.	n.a.
Total	1.00	1.00	1.00	1.00	1.00	4.00	3.99	3.99	4.01	4.01
Mg#	0.94	0.92	0.91	0.98	0.95	0.82	0.81	0.81	0.82	0.81

TABLE 1. REPRESENTATIVE CATION DATA AND CALCULATED TEMPERATURES AS A FUNCTION OF ROCK TYPE

Rock type Sample	Fe cpx	Mg cpx	Ca cpx	Na cpx	Fe opx	Mg opx	Ca opx	Na opx	T @ 1.5 GPa*	Comments[†]
Spinel lherzolite										
CSR-8	0.075	0.869	0.866	0.072	0.172	1.706	0.021	0.002	842	
	0.079	0.867	0.852	0.073	0.173	1.724	0.025	0.003	899	
CG-38	0.089	0.856	0.801	0.095	0.175	1.697	0.028	0.006	996	
	0.086	0.864	0.806	0.096	0.175	1.708	0.025	0.006	976	
CTON-53	0.052	0.905	0.862	0.046	0.164	1.706	0.027	0.003	953	
	0.084	0.902	0.86	0.047	0.164	1.706	0.027	0.003	956	
	0.087	0.953	0.737	0.063	0.164	1.716	0.026	0.002	1176	Adjacent to melt pocket
CTON-57	0.081	0.897	0.858	0.04	0.166	1.699	0.026	0.002	979	Megacryst
	0.084	0.888	0.864	0.041	0.148	1.513	0.024	0.002	959	Megacryst
	0.079	0.904	0.864	0.041	0.164	1.709	0.027	0.002	960	
	0.08	0.894	0.864	0.04	0.163	1.695	0.027	0.002	963	
Cr-diopside pyroxenite										
CTON-21	0.081	0.864	0.836	0.072	0.203	1.702	0.02	0.004	943	
	0.083	0.843	0.836	0.073	0.206	1.664	0.02	0.002	939	
	0.081	0.864	0.836	0.072	0.193	1.64	0.067	0.007	958	
	0.081	0.848	0.826	0.076	0.188	1.61	0.096	0.009	988	Fine exsolution
	0.083	0.888	0.818	0.067	0.199	1.673	0.026	0.006	1003	Opx in melt inclusion in cpx
	0.08	0.868	0.844	0.072	0.162	1.43	0.285	0.024	1015	Opx in melt inclusion in cpx
CTON-67	0.084	0.803	0.831	0.074	0.214	1.609	0.019	0.003	947	
	0.086	0.805	0.826	0.076	0.212	1.604	0.021	0.004	959	
	0.083	0.796	0.83	0.076	0.21	1.613	0.019	0.003	946	
	0.082	0.807	0.828	0.077	0.208	1.606	0.02	0.003	950	
	0.084	0.792	0.827	0.08	0.213	1.609	0.019	0.002	945	
	0.086	0.801	0.834	0.075	0.212	1.61	0.02	0.003	936	
Spinel pyroxenite										
CTON-5	0.086	0.827	0.826	0.079	0.216	1.656	0.02	0.002	950	
	0.087	0.833	0.842	0.079	0.216	1.662	0.02	0.002	900	
	0.086	0.819	0.82	0.082	0.214	1.634	0.019	0.003	960	
Garnet pyroxenite										
CTON-6	0.219	0.704	0.751	0.113	0.392	1.453	0.067	0.008	1000	
	0.214	0.73	0.747	0.108	0.392	1.453	0.037	0.008	1014	
CTON-17	0.206	0.737	0.736	0.098	0.356	1.45	0.04	0.01	1057	
	0.213	0.715	0.729	0.097	0.371	1.401	0.037	0.008	1058	Coarse exsolution
	0.212	0.718	0.722	0.099	0.367	1.408	0.039	0.009	1067	Coarse exsolution
	0.219	0.731	0.718	0.099	0.373	1.407	0.04	0.008	1071	Coarse exsolution
CTON-77	0.247	0.716	0.709	0.115	0.385	1.342	0.067	0.008	1064	
	0.234	0.718	0.714	0.114	0.411	1.42	0.067	0.008	1056	
CTON-81	0.218	0.738	0.701	0.111	0.416	1.349	0.072	0	1064	Rim around gar symplectite
	0.212	0.739	0.727	0.105	0.353	1.348	0.066	0.004	1051	Rim around gar symplectite
	0.232	0.757	0.695	0.088	0.411	1.258	0.096	0.001	1107	Rim around gar symplectite
	0.217	0.719	0.714	0.108	0.382	1.447	0.035	0.009	1065	Coarse exsolution blebs
	0.218	0.707	0.724	0.107	0.391	1.436	0.035	0.009	1050	Coarse exsolution blebs
	0.223	0.711	0.715	0.105	0.389	1.433	0.032	0.008	1073	Coarse exsolution blebs
Carbonate-bearing pyroxenite										
CTON-2	0.199	0.822	0.735	0.078	0.338	1.505	0.048	0.009	1091	Coarse exsolution blebs
	0.196	0.825	0.732	0.078	0.344	1.502	0.049	0.008	1092	Coarse exsolution blebs
	0.201	0.838	0.72	0.075	0.334	1.491	0.066	0.009	1116	Coarse exsolution blebs
CTON-7	0.822	0.198	0.735	0.09	0.336	1.52	0.047	0.006	1144	Rxn halo around carb melt
	0.842	0.187	0.745	0.087	0.333	1.497	0.048	0.009	1134	Opx in carb melt incl in cpx
	0.826	0.189	0.739	0.085	0.342	1.484	0.049	0.008	1140	Opx in carb melt incl in cpx
CTON-13	0.192	0.817	0.749	0.083	0.328	1.476	0.047	0.008	1067	Opx in carb melt incl in cpx
CG-30	0.225	0.717	0.738	0.097	0.421	1.403	0.034	0.007	1028	
	0.23	0.716	0.738	0.099	0.42	1.406	0.034	0.006	1025	Coarse exsolution
	0.227	0.705	0.742	0.1	0.427	1.401	0.036	0.007	1030	Opx in carb melt incl in cpx
CG-40	0.275	0.689	0.661	0.121	0.459	1.353	0.047	0.013	1083	
	0.271	0.715	0.691	0.112	0.436	1.347	0.045	0.01	1066	
	0.263	0.731	0.684	0.109	0.41	1.406	0.05	0.009	1092	Opx in carb melt incl in cpx

Note: opx—orthopyroxene, cpx—clinopyroxene, gar—garnet, rxn—reaction, carb—carbonate, incl—inclusion.
 *Temperatures (°C) were calculated using the two-pyroxene thermometer of Brey and Köhler (1990) at a reference pressure of 1.5 GPa.
 [†]All analyses are from adjacent matrix grains unless otherwise stated.
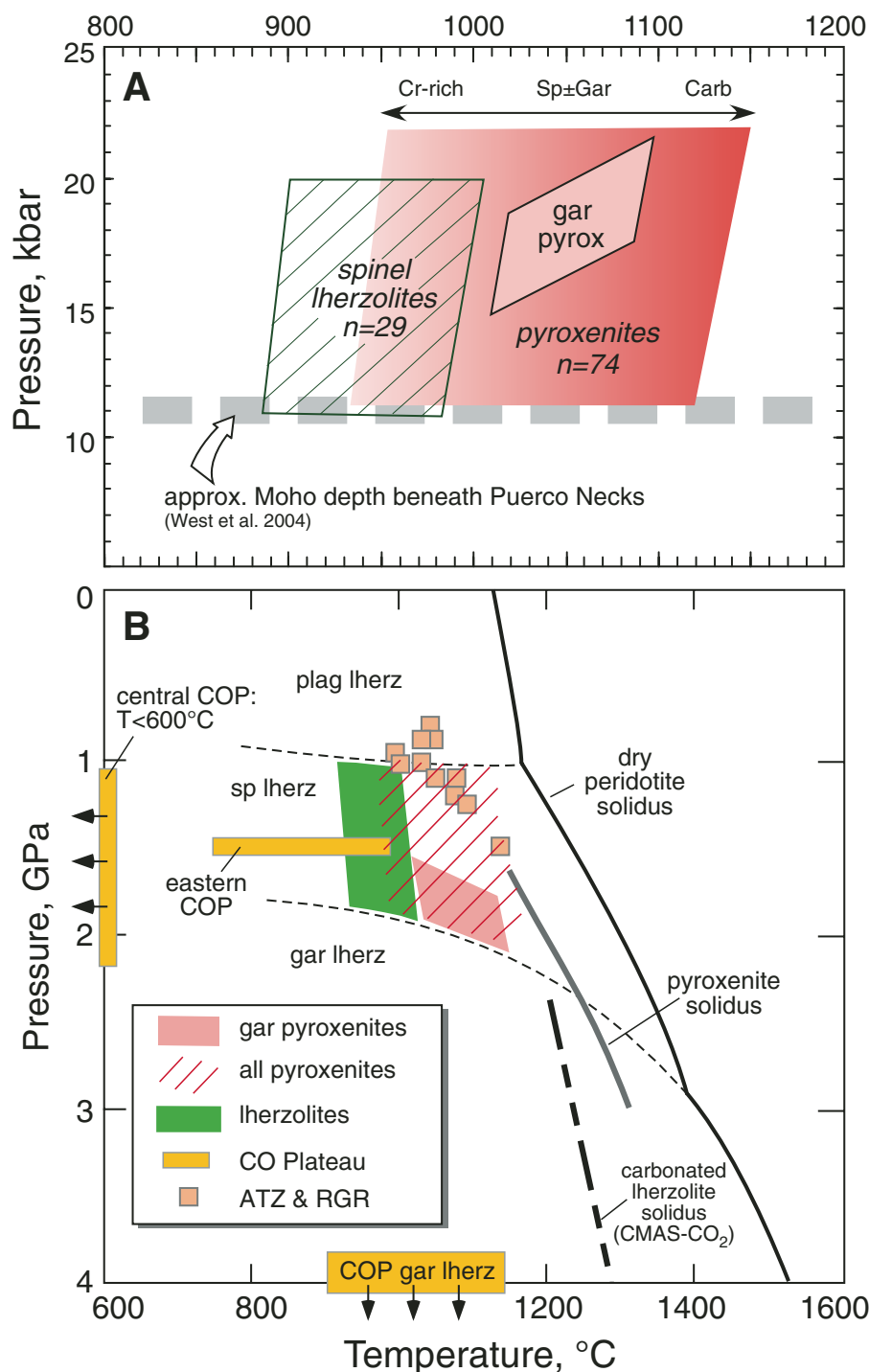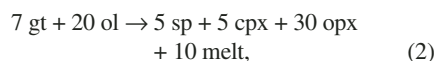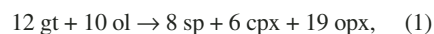
Figure 14. (A) Temperature ranges calculated for spinel lherzolites and pyroxenites from Rio Puerco necks, using the two-pyroxene thermometer of Brey and Köhler (1990). Cr-diopside pyroxenites overlap lherzolite temperature range, most spinel ± garnet pyroxenites record temperatures around 1050 ± 50 °C, and carbonate-bearing pyroxenites record temperatures in excess of 1100 °C. Quadrilateral inset into pyroxenite field indicates range of pressure-temperature conditions calculated from garnet-bearing pyroxenites CTON-6 and CTON-77. (B) Pressure-temperature conditions of Rio Puerco xenoliths compared to xenoliths from the Colorado Plateau (COP; Smith and Barron, 1991; Riter and Smith, 1996; Smith, 2000) and the Rio Grande rift (RGR) and Arizona Transition Zone (ATZ; Baldridge, 1979; McGuire, 1994; Smith, 2000). Pyroxenite solidus is from Pertermann and Hirschmann (2003); carbonated lherzolite solidus is from Gudfinnsson and Presnall (2005).

record modifications to the lithosphere below the Rio Puerco necks after initial formation of the pyroxenites.

Garnet Breakdown

In the garnet-bearing pyroxenite samples, relict garnet grains are surrounded by reaction rims up to 200 μm in width. Petrographic and microprobe data indicate that the reaction zones are composed of orthopyroxene, spinel, clino-pyroxene, and silicate glass. Anorthite is locally present, but it is probably a product of subsequent breakdown of the spinel. As is evident in Figure 10, orthopyroxene is by far the most abundant phase in the symplectites rimming garnet, with lesser but subequal amounts of spinel, clinopyroxene, and glass.

Using average compositions of matrix clinopyroxene, relict garnet, symplectite orthopyroxene, spinel, plagioclase, and glass from the garnet pyroxenites, along with olivine data from the lherzolite samples, the following three balanced reactions were calculated (coefficients on a molar basis, see Table 3 for volumetric proportions):

$$12 \, gt + 10 \, ol \rightarrow 8 \, sp + 6 \, cpx + 19 \, opx, \quad (1)$$

$$7 \, gt + 20 \, ol \rightarrow 5 \, sp + 5 \, cpx + 30 \, opx + 10 \, melt, \quad (2)$$

$$13 \, gt + 10 \, melt \rightarrow 5 \, cpx + 4 \, opx + 9 \, sp. \quad (3)$$

These reactions are obviously simplifications in that they do not allow for continuous changes in composition of the phases. Nonetheless, they provide a starting point for evaluating the reaction histories of these samples. Both reactions 1 and 2 imply derivation of the reaction zones from an olivine-bearing precursor in which olivine is the limiting reactant. Reaction 1 predicts production of orthopyroxene in ~3:1 volumetric proportions relative to both spinel and clinopyroxene, with no involvement of a melt phase. Reaction 2 more closely approximates the observed phase abundances shown in Figure 10, including glass preserved within the symplectites and the high modal production of orthopyroxene. There is poor agreement between the observed abundances and those predicted by reaction 3. One possible interpretation of the reaction zones thus involves closed-system, in situ partial melting of an olivine-bearing garnet pyroxenite, resulting in total consumption of olivine and production of two pyroxenes, spinel, and quenched glass.

Glass inclusions with the highest MgO contents were used with the pMELTS program

(Ghiorso et al., 2002) to determine the approximate solidus temperature of the melt involved in reaction 2. Calculations at a reference pressure of 1.5 GPa yielded solidus temperatures ranging from 1050 °C (fO_2 = QFM +1.0 log unit) to 1100 °C (fO_2 = QFM −1.0 log unit). In all cases, calculated mineral compositions and modes were similar to those observed in the actual assemblages. These calculations support garnet breakdown via localized partial melting at the temperatures and pressures calculated for the samples.

Spinel Breakdown

Black spinel grains, which are abundant in the garnet-bearing samples, are surrounded by 50–100-μm-wide reaction rims composed of orthopyroxene, anorthite, and glass (Fig. 11). Textural analyses coupled with microprobe data give rise to the following balanced reaction (mol%; see Table 3 for vol%):

$$6\ sp + 6\ cpx \rightarrow 13\ opx + 5\ an + 10\ melt. \quad (4)$$

Product phase abundances predicted from this reaction are in reasonable agreement with the relative abundances of orthopyroxene and plagioclase in the reaction rims; however, the amount of melt varies significantly within and between symplectites in all samples in which glass is observed.

In order to evaluate the pressure-temperature dependence of the breakdown reactions, thermodynamic data were calculated from microprobe data for all phases using the MELTS Supplemental Calculator (http://melts.ofm-research.org/CalcForms/index.html; Ghiorso and Sack, 1995; Ghiorso and Kress, 2004) at reference conditions of 1100 °C and 1.5 GPa (Table 3). Reaction 1 has a shallow slope of 5 bar/°C and thus requires decompression to proceed. Reactions 2–4 have steeper slopes (45, −108, and 70 bars/°C, respectively). Hence, garnet breakdown via reaction 2 and spinel breakdown via reaction 4 both likely occurred in response to a combination of heating and decompression (Fig. 16).

Timing of Pyroxenite Formation and Garnet-Spinel Breakdown Reactions

Pyroxenite xenoliths are also abundant in Pleistocene (Anthony and Poths, 1992) eruptive materials at Kilbourne Hole and Potrillo Maar in the southern portion of the Rio Grande rift (Irving, 1980; Wilshire et al., 1988; Padovani and Reid, 1989), although carbonate has not been reported from these pyroxenites. No pyroxenites were observed in the mantle xenolith suite from the Cieneguilla limburgite, a locality in the center of the Rio Grande rift that was emplaced

TABLE 2. WHOLE-ROCK AND NORMATIVE COMPOSITIONS OF LHERZOLITE AND PYROXENITE XENOLITHS

Neck	CN	CTON	CSR	CSR	CSR	CSR	CSR	CSR	CSR	CG	CG	CTON	CTON	CTON	CTON	CTON	CTON	CTON	CV	CSR
Sample		53	17	20	27	45	47	49	87	16	38	2	4	04	106	108	111	99	12	5B
Rock type	lherz	lherz	lherz	lherz	lherz	lherz	lherz	lherz	lherz	lherz	lherz	pyrox	pyrox	pyrox	pyrox	pyrox	pyrox	pyrox	pyrox	pyrox
SiO₂	43.92	44.21	42.34	43.35	42.92	42.87	41.65	42.07	43.89	42.83	43.03	51.11	51.29	38.96	48.12	48.19	49.62	46.94	43.55	33.43
TiO₂	0.04	0.04	0.08	0.05	0.04	0.06	0.06	0.05	0.05	0.12	0.09	0.64	0.83	1.27	0.86	0.78	0.68	1.08	0.46	0.41
Al₂O₃	2.67	2.1	2.71	2.6	2.87	2.18	1.98	2.06	2.31	3.93	3.22	7.22	8.38	17.22	8.59	8.36	7.3	9.08	13.86	24.08
Fe₂O₃*	9.44	8.92	10.37	9.43	9.55	9.07	10.31	9.48	8.99	9.73	9.81	8.34	8.75	11.76	9.05	7.9	8.39	9.93	9.26	14.16
MnO	0.14	0.13	0.16	0.14	0.14	0.14	0.15	0.14	0.13	0.14	0.15	0.16	0.15	0.13	0.16	0.15	0.15	0.15	0.16	0.17
MgO	40.48	38.68	38.26	40.05	39.55	39.2	39.31	40.91	39.64	37.51	37.83	16.5	16.15	13.6	15.34	15.07	16.47	15.45	15.16	16.41
CaO	1.97	3.02	2.62	1.7	1.88	1.95	2.03	1.94	2.13	3.08	2.58	14.42	14.39	14.23	15.08	16.26	15.26	14.21	13.36	8.25
Na₂O	0	0	0.1	0	0.09	0	0	0	0	0.12	0.07	0.94	1.13	1.06	0.99	0.95	0.89	0.97	1.05	0.69
K₂O	0	0	0.04	0.01	0.01	0	0	0	0	0.06	0	0	0.01	0	0	0	0	0	0.13	0.02
P₂O₅	0	0	0.01	0	0	0.04	0.04	0.04	0.04	0.01	0.01	0.04	0.05	0.01	0	0.01	0.01	0.01	0.02	0
LOI	0.68	1.22	0.47	0.46	0	0.54	0.58	0.41	0.37	0.61	1.5	0.53	0.91	1.04	1.21	1.39	0.79	1.52	1.66	1.15
Total	99.34	98.33	97.16	97.77	97.04	96.03	96.11	97.11	97.53	98.15	98.28	99.9	102.03	99.27	99.38	99.05	99.56	99.32	98.67	98.76
Mg#	0.9	0.9	0.88	0.89	0.089	0.9	0.88	0.9	0.91	0.88	0.88	0.8	0.79	0.7	0.77	0.79	0.8	0.76	0.76	0.7
CaO/Al₂O₃	0.74	1.44	0.97	0.66	0.66	0.89	1.03	0.94	0.92	0.78	0.8	2	1.72	0.83	1.76	1.94	2.09	1.57	0.96	0.34
qz	0	0	0	0	0	0	0	0	0	0	0	2.3	1.4	0	0	0	0.1	0	0	0.7
pl	7.3	5.7	7.7	7.1	8.2	6	5.4	5.6	6.3	11	9.1	23.4	27.3	43.6	27.4	26.6	23.5	28.6	41.6	45.5
or	0	0	0.2	0.1	0.1	0	0	0	0	0.4	0	0	0.1	0	0	0	0	0	0.8	0.1
ne	0	0	0	0	0	0	0	0	0	0	0	0	0	4.1	0	0	0	0	0	0.7
di	1.9	7.2	4.8	1.1	1.5	2.7	3.4	2.9	3.1	4.1	3.3	42.2	39.7	19	41.6	46.7	45.1	36.5	25.3	0
en	32.7	33.1	27.3	33.3	30.3	33.3	28.7	26.5	34.5	26.5	31.4	21.5	21.8	0	16.4	11.9	20.1	17.1	2.6	0
ol	47.1	42	46.1	46.2	47.3	44.2	47.4	51.9	44	45.6	43	0	0	17.6	1.8	2.8	0	3.2	16.4	28.6

Note: LOI—loss on ignition, lherz—lherzolite, pyrox—pyroxene, qz—quartz, pl—plagioclase, or—orthoclase, ne—nepheline, di—diopside, en—enstatite, ol—olivine.
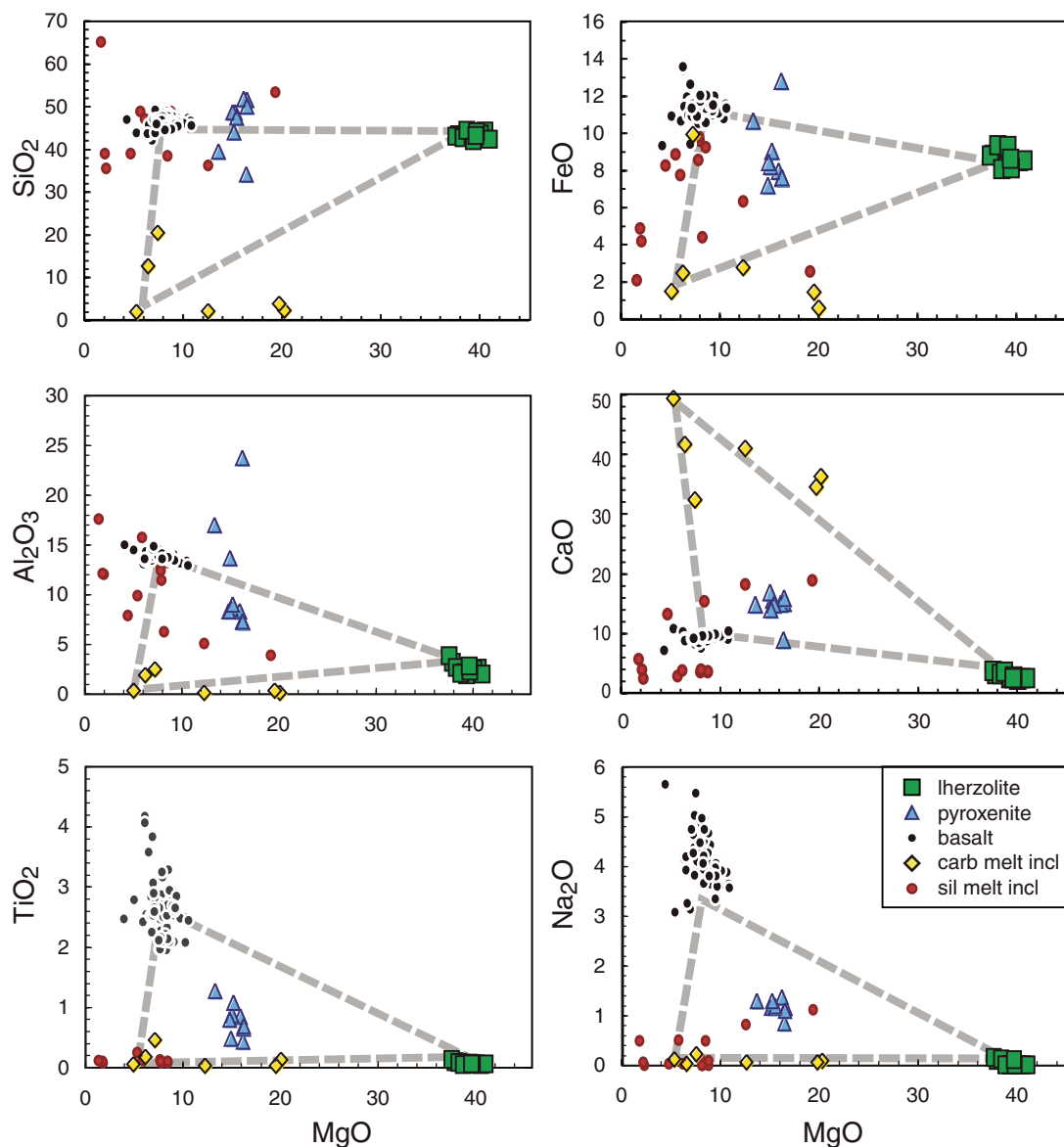*All iron is reported as Fe₂O₃.

Figure 15. Major-element compositions of Rio Puerco basalts (Hallett, 1994) and lherzolites, pyroxenites, silicate (sil) melt inclusions, and carbonate (carb) melt inclusions from this study. Dashed lines connect basalt with 8% MgO, average lherzolite, and most calcic carbonate melt inclusion as reference for three-phase mixing estimates.

early in the extensional history (ca. 25 Ma) (Baldridge, 1979; Baldridge et al., 1980). Initial generation of the silicate ± carbonatite melts responsible for converting lherzolite into pyroxenite likely occurred in response to lithospheric thinning and/or asthenospheric upwelling associated with rifting. Oxygen isotopic disequilibrium between pyroxenes and olivine in lherzolites and between pyroxenes and calcite in pyroxenites constrains the youngest carbonatite-silicate melt metasomatic events to <1 m.y. prior to eruption in the Puerco field (Perkins et al., 2006). Preservation of fine-scale zoning in carbonate grains is also consistent with metasomatism occurring just prior to sampling by the host magmas. The preservation of different xenolith populations in volcanic centers of different age thus roughly constrains melt-peridotite interaction to

Miocene-Pleistocene along the Rio Grande rift, and to the Pliocene for the region beneath the Rio Puerco necks.

Garnet breakdown within the pyroxenites obviously must postdate pyroxenite formation, and must thus record mantle processes shortly before eruption of the host basalts. The symplectite reaction rims around garnet reach up to 200 μm in diameter and are overprinted by symplectites derived from spinel breakdown. Geobarometric calculations yield lower pressures for the samples with wide reaction rims compared to those with narrower rims. The reaction was most likely driven by heating related to melt passage through the mantle source region, combined with rift-related decompression. The narrower symplectite zones surrounding spinel, coupled with the development of plagioclase in

these zones, suggest that spinel breakdown may have occurred during ascent in the host magma.

TECTONIC SUMMARY

Mantle-derived pyroxenites occur only locally within xenolith suites from the Colorado Plateau (e.g., McGetchin and Silver, 1972), but are abundant in xenolith suites from the southern Rio Grande rift (e.g., Irving, 1980; Wilshire et al., 1988) and the Rio Puerco necks (this study). This association is not surprising if pyroxenite formation results from melt-rock interaction, since the warm mantle of the extended regions of the western United States provides greater opportunity for such interactions than does the cooler mantle beneath the Colorado Plateau. The Rio Puerco pyroxenites differ in two significant respects from

other pyroxenites in the western United States; however, calcite and carbonate melt inclusions are abundant, and pyroxene compositions are more extreme than those of pyroxenites within the southern Rio Grande rift (e.g., Fig. 5). The calcite and the carbonate melt inclusions point to involvement of carbonatitic melts in the evolution of the Rio Puerco mantle, and the pyroxene compositions imply that this mantle region was more extensively metasomatized than the mantle beneath the southern Rio Grande rift. The mantle beneath the Colorado Plateau also experienced pervasive metasomatism, but largely in response to infiltration of hydrous fluids thought to be related to subduction of the Farallon slab (e.g., Smith et al., 1999, 2004; Smith and Griffin, 2005). Magnesite has been reported in a few peridotite xenoliths from Green Knobs on the Colorado Plateau (Smith, 1979) but is not prevalent. Likewise, hydrous minerals (phlogopite, amphibole, and apatite) occur within some of the Rio Puerco xenoliths (Samuels et al., 2006) but are rare. These observations suggest that the composition of the metasomatizing fluid(s), the extent of metasomatic interaction, and the thermal history all differed between the mantle beneath the Colorado Plateau, the Rio Puerco necks, and the southern Rio Grande rift.

On the basis of stable isotopic data, Perkins et al. (2006) argued that carbonatitic melts in the Rio Puerco field originated from mantle that had interacted with fluids derived from the subducted Farallon plate. Ducea et al. (2005) reached a similar conclusion from isotopic analysis of carbonate inclusions in peridotite xenoliths from the Sierra Nevada. Although the Farallon plate is thought to have detached and sunk to depth between 50 and 20 Ma (Humphreys, 1995), its chemical influence is still apparent within recently modified mantle samples from the Puerco necks (Fig. 16) as well as the hydrated xenoliths from Tertiary eruptions on the Colorado Plateau (Smith et al., 2004; Smith and Griffin, 2005). One possible explanation for the high degree of melt metasomatism in this region comes from the location of the Puerco necks at the intersection between the Rio Grande rift and the Jemez Lineament. Although the Jemez Lineament is defined as an alignment of Cenozoic volcanic centers, it likely reflects a lithospheric discontinuity of Precambrian ancestry (Karlstrom and Humphreys, 1998). It is currently underlain by seismically slow mantle, indicating anomalously high temperatures, the presence of partial melt, and/or local variations in hydration or other chemical heterogeneity (Gao et al., 2004). If the Jemez Lineament is truly a lithospheric-scale structure, variations in fracture density at depth may have focused fluids/melts released from the subducting Farallon plate into
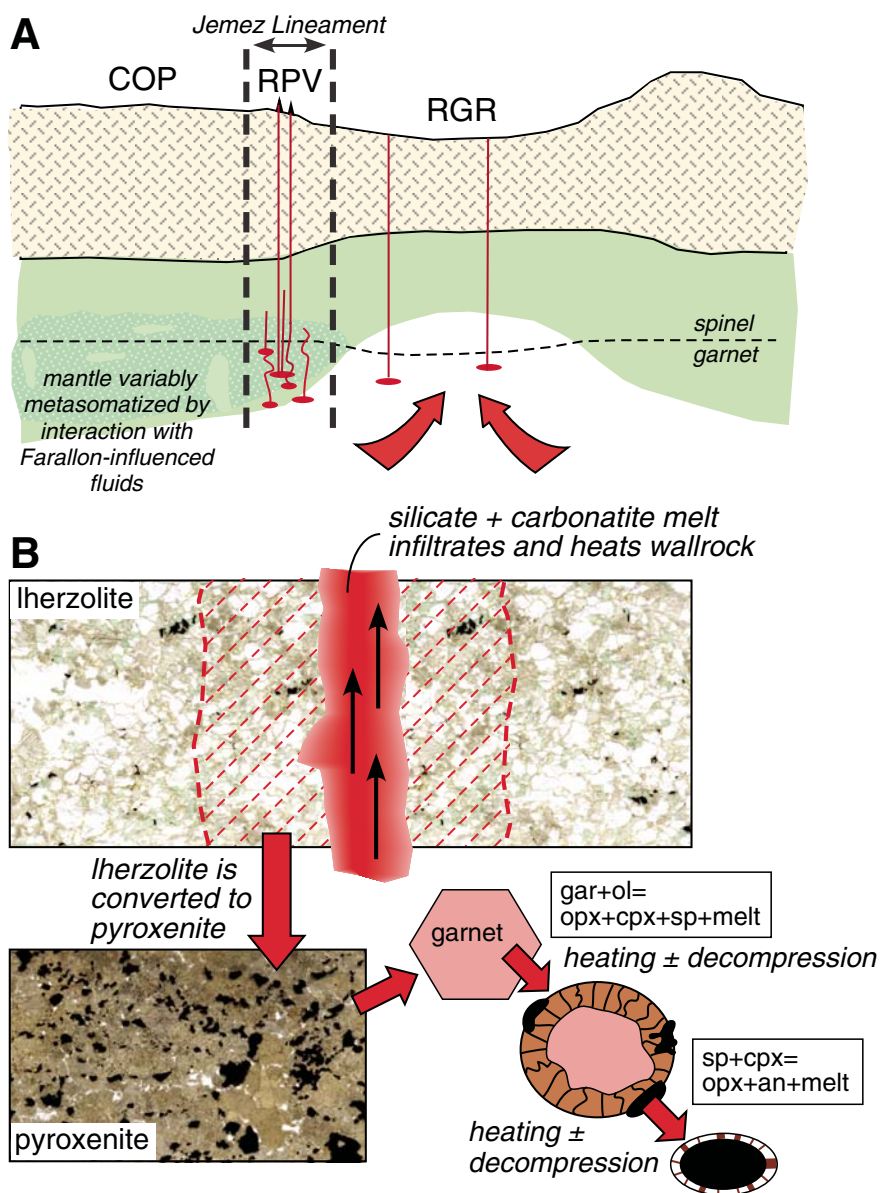
Figure 16. Cartoons illustrating setting and probable origin of Rio Puerco pyroxenite xenoliths. (A) Tectonic setting of Rio Puerco volcanic (RPV) field on margin of Rio Grande rift (RGR) and within the Jemez Lineament. Source region for pyroxenite xenoliths is more extensively modified by interaction with silicate + carbonatite melts than xenolith source areas beneath the Colorado Plateau (COP) or the Rio Grande rift, suggesting that Jemez Lineament may localize metasomatizing melts at depth. (B) Lherzolite is converted to pyroxenite via melt-rock interaction adjacent to melt conduits, probably less than 1 m.y. before xenolith entrainment. Garnet (gar) forms in areas of extensive melt infiltration and subsequently breaks down in response to continued heating and decompression during rifting. Spinel (sp) also breaks down in response to heating ± decompression, either in situ or during ascent in host basalt. Abbreviations: opx—orthopyroxene, cpx—clinopyroxene, ol—olivine, an—anorthite.

this zone. Asthenospheric upwelling following Farallon removal would then have led to enhanced melt production within the metasomatized mantle of the region and to entrainment of a wide variety of xenolith types. This hypothesis requires further testing through more detailed studies of pyroxenite xenoliths from localities that lie outside of the Jemez Lineament.

Regardless of the fluid-focusing mechanisms at depth, the pyroxenites of the Rio Puerco necks preserve a record of silicate and carbonatite melt metasomatism, heating, and decompression in

TABLE 3. STOICHIOMETRIC COEFFICIENTS AND THERMODYNAMIC DATA FOR
GARNET PYROXENITE REACTIONS

	Gar	Sp	Opx	Cpx	Oliv	Plag	Melt	dP/dT (bar K^{-1})
Stoichiometric coefficients								
Reaction 1	−12	8	19	6	−10			5
Reaction 2	−7	5	30	5	−20		10	45
Reaction 3	−13	9	4	5			−10	−108
Reaction 4		−6	13	−6		5	10	70
Volumetric proportions								
Reaction 1		17	62	20				
Reaction 2		8	69	12			11	
Reaction 3		39	26	34				
Reaction 4			43			25	33	
Thermodynamic data								
(cm^3)	118.7	41.2	67.0	66.7	45.3	100.6	30.8	
(J K^{-1})	985.4	358.2	534.5	499.5	337.8	642.3	220.9	

Note: Reactions were balanced using average compositions determined by microprobe analysis. Negative coefficients indicate reactants; positive values indicate product phases. Volumetric data are normalized to 100% products. Molar volume and entropy data were calculated using MELTS supplemental calculator (http://melts.ofm–research.org/CalcForms/index.html) at reference conditions of 1100 °C and 15 kbar. Gar—garnet, Sp—spinel, Opx—orthopyroxene, Cpx—clinopyroxene, Oliv—olivine, Plag—plagioclase.

the upper mantle at the junction of the Colorado Plateau and the Rio Grande rift. The LA RISTRA experiment documented pronounced seismic attenuation to depths ≥200 km in the mantle beneath this area. Gao et al. (2004) interpreted the low velocities in terms of thermal erosion of the lithosphere, but cautioned that the data could not rule out the presence of small amounts of melt and/or hydration. The textural and pressure-temperature data from the Rio Puerco garnet pyroxenites support both heating and decompression within the lithospheric mantle prior to entrainment in the host basalts. These data are in accord with a model in which lithosphere is thinned and thermally converted to asthenosphere. However, the high degree of melt-rock interaction recorded by the entire pyroxenite suite is also consistent with pervasive chemical modification of the lithosphere. Conversion of a significant amount of lherzolite to clinopyroxene-rich pyroxenite with lower bulk Mg number will result in significant reduction in seismic-wave velocities. Chemical modification of the mantle may thus be as important as temperature effects in explaining the low-velocity zone beneath the Puerco necks. If the seismic anomaly in this region does result in large part from chemical effects, we predict that the extensively refertilized lithosphere will ultimately become negatively buoyant, once rift-related heating comes to an end (e.g., Carlson et al., 2005).

ACKNOWLEDGMENTS

REFERENCES CITED

Aldrich, M.J., and Laughlin, A.W., 1984, A model for the tectonic development of the southeastern Colorado Plateau boundary: Journal of Geophysical Research, v. 89, p. 10,207–10,218.

Anthony, E.Y., and Poths, J., 1992, He³ surface exposure dating and its implications for magma evolution in the Potrillo volcanic field, Rio Grande rift, New Mexico, USA: Geochimica et Cosmochimica Acta, v. 56, no. 11, p. 4105–4108, doi: 10.1016/0016-7037(92)90022-B.

Baldridge, W.S., 1979, Mafic and ultramafic inclusion suites from the Rio Grande rift (New Mexico) and their bearing on the composition and thermal state of the lithosphere: Journal of Volcanology and Geothermal Research, v. 6, no. 3–4, p. 319–351, doi: 10.1016/0377-0273(79)90009-X.

Baldridge, W.S., Damon, P.E., Shafiqullah, M., and Bridwell, R.J., 1980, Evolution of the central Rio Grande rift, New Mexico: New potassium-argon ages: Earth and Planetary Science Letters, v. 51, no. 2, p. 309–321, doi: 10.1016/0012–821X(80)90213–7.

Baldridge, W.S., Perry, F.V., Vaniman, D.T., Nealey, L.D., Leavy, B.D., Laughlin, A.W., Kyle, P., Bartov, Y., Steinitz, G., and Gladney, E.S., 1991, Middle to Late Cenozoic magmatism of the southeastern Colorado Plateau and central Rio Grande rift (New Mexico and Arizona, USA): A model for continental rifting: Tectonophysics, v. 197, no. 2–4, p. 327–354, doi: 10.1016/0040-1951(91)90049-X.

Brey, G.P., and Köhler, T., 1990, Geothermobarometry in 4-phase lherzolites, 2. New thermobarometers and practical assessment of existing thermobarometers: Journal of Petrology, v. 31, p. 1353–1378.

Carlson, R.W., and Nowell, G.M., 2001, Olivine-poor sources for mantle-derived magmas: Os and Hf isotopic evidence from potassic magmas of the Colorado Plateau: Geochemistry, Geophysics, Geosystems, v. 2, p. U33–U49, doi: 10.1029/2000GC000128.

Carlson, R.W., Pearson, D.G., and James, D.E., 2005, Physical, chemical, and chronological characteristics of continental mantle: Reviews of Geophysics, v. 43, p. RG1001, doi: 10.1029/2004RG000156.

Coney, P., and Reynolds, S., 1977, Flattening of the Farallon slab: Nature, v. 270, p. 403–406, doi: 10.1038/270403a0.

Dickinson, W., and Snyder, W.S., 1978, Plate tectonics of the Laramide orogeny, in Matthews, V., III, ed., Laramide Folding Associated with Basement Block Faulting in the Western United States: Geological Society of America Memoir 151, p. 355–366.

Dobosi, G., Downes, H., Embey-Isztin, A., and Jenner, G.A., 2003, Origin of megacrysts and pyroxenite xenoliths from the Pliocene alkali basalts of the Pannonian Basin (Hungary): Neues Jahrbuch für Mineralogie-Abhandlungen, v. 178, no. 3, p. 217–237, doi: 10.1127/0077-7757/2003/0178-0217.

Downes, H., 2001, Formation and modification of the shallow sub-continental lithospheric mantle: A review of geochemical evidence from ultramafic xenolith suites and tectonically emplaced ultramafic massifs of western and central Europe: Journal of Petrology, v. 42, no. 1, p. 233–250, doi: 10.1093/petrology/42.1.233.

Droop, G., 1987, A general equation for estimating Fe³⁺ concentrations in ferromagnesian silicates and oxides from microprobe analyses: Mineralogical Magazine, v. 51, p. 431–435.

Ducea, M.N., and Saleeby, J.B., 1996, Buoyancy sources for a large, unrooted mountain range, the Sierra Nevada, California: Evidence from xenolith thermobarometry: Journal of Geophysical Research, v. 101, p. 8229–8244, doi: 10.1029/95JB03452.

Ducea, M., Saleeby, J., Morrison, J., and Valencia, V., 2005, Subducted carbonates, metasomatism of mantle wedges, and possible connections to diamond formation: An example from California: The American Mineralogist, v. 90, p. 864–870, doi: 10.2138/am.2005.1670.

Dueker, K., Yuan, H., and Zurek, B., 2001, Thick-structured Proterozoic lithosphere of the Rocky Mountain region: GSA Today, v. 11, no. 12, p. 4–9, doi: 10.1130/1052-5173(2001)011<0004:TSPLOT>2.0.CO;2.

Gao, W., Grand, S.P., Baldridge, W.S., Wilson, D., West, M., Ni, J.F., and Aster, R., 2004, Upper mantle convection beneath the central Rio Grande rift imaged by P and S wave tomography: Journal of Geophysical Research, v. 109, no. B3, p. B03305, doi: 10.1029/2003JB002743.

Garrido, C.J., and Bodinier, J.L., 1999, Diversity of mafic rocks in the Ronda peridotite: Evidence for pervasive melt-rock reaction during heating of subcontinental lithosphere by upwelling asthenosphere: Journal of Petrology, v. 40, no. 5, p. 729–754, doi: 10.1093/petrology/40.5.729.

Ghiorso, M.S., and Kress, V.C., 2004, An equation of state for silicate melts. II. Calibration of volumetric properties at 10(5) Pa: American Journal of Science, v. 304, no. 8–9, p. 679, doi: 10.2475/ajs.304.8-9.679.

Ghiorso, M.S., and Sack, R.O., 1995, Chemical mass-transfer in magmatic processes. 4. A revised and internally consistent thermodynamic model for the interpolation and extrapolation of liquid-solid equilibria in magmatic systems at elevated temperatures and pressures: Contributions to Mineralogy and Petrology, v. 119, no. 2–3, p. 197–212.

Ghiorso, M.S., Hirschmann, M.M., Reiners, P.W., and Kress, V.C., 2002, The pMELTS: A revision of MELTS for improved calculation of phase relations and major element partitioning related to partial melting of the mantle to 3 GPa: Geochemistry, Geophysics, Geosystems, v. 3, no. 5, doi: 10.1029/2001GC000217.

Gudfinnsson, G.H., and Presnall, D.C., 2005, Continuous gradations among primary carbonatitic, kimberlitic, melilititic, basaltic, picritic, and komatiitic melts in equilibrium with garnet lherzolite at 3–8 GPa: Journal of Petrology, v. 46, no. 8, p. 1645, doi: 10.1093/petrology/egi029.

Hallett, R.B., 1994, Volcanic geology, paleomagnetism, geochronology, and geochemistry of the Rio Puerco necks, west-central New Mexico [Ph.D. thesis]: Socorro, New Mexico Institute of Mining and Technology, 340 p.

Hallett, R.B., Kyle, P.R., and McIntosh, W.C., 1997, Paleomagnetic and Ar-40/Ar-39 age constraints on the chronologic evolution of the Rio Puerco volcanic necks and Mesa Prieta, west-central New Mexico: Implications for transition zone magmatism: Geo-

logical Society of America Bulletin, v. 109, no. 1, p. 95–106, doi: 10.1130/0016-7606(1997)109<0095: PAAAAC>2.3.CO;2.

Hart, S.R., and Dunn, T., 1993, Experimental clinopyroxene-melt partitioning of 24 trace elements: Contributions to Mineralogy and Petrology, v. 113, p. 1–8, doi: 10.1007/BF00320827.

Henjes-Kunst, F., and Altherr, R., 1992, Metamorphic petrology of xenoliths from Kenya and northern Tanzania and implications for geotherms and lithospheric structures: Journal of Petrology, v. 33, no. 5, p. 1125–1156.

Hirschmann, M.M., and Stolper, E.M., 1996, A possible role for garnet pyroxenite in the origin of the "garnet signature" in MORB: Contributions to Mineralogy and Petrology, v. 124, no. 2, p. 185–208, doi: 10.1007/s004100050184.

Hirschmann, M.M., Kogiso, T., Baker, M.B., and Stolper, E.M., 2003, Alkalic magmas generated by partial melting of garnet pyroxenite: Geology, v. 31, no. 6, p. 481–484, doi: 10.1130/0091-7613(2003)031<0481: AMGBPM>2.0.CO;2.

Ho, K.S., Chen, J.C., Smith, A.D., and Juang, W.S., 2000, Petrogenesis of two groups of pyroxenite from Tungchihsu, Penghu Islands, Taiwan Strait: Implications for mantle metasomatism beneath SE China: Chemical Geology, v. 167, no. 3–4, p. 355–372, doi: 10.1016/S0009-2541(99)00237-5.

Humphreys, E., and Dueker, K., 1994, Physical state of the western U.S. upper mantle: Journal of Geophysical Research, v. 99, p. 9635–9650, doi: 10.1029/93JB02640.

Humphreys, E.D., 1995, Post-Laramide removal of the Farallon Slab, western United States: Geology, v. 23, no. 11, p. 987–990, doi: 10.1130/0091-7613(1995)023<0987: PLROTF>2.3.CO;2.

Humphreys, E.D., Hessler, E., Dueker, K., Farmer, C.L., Erslev, E., and Atwater, T., 2003, How Laramide-age hydration of North American lithosphere by the Farallon slab controlled subsequent activity in the western United States: International Geology Review, v. 45, no. 7, p. 575–595.

Irving, A., 1980, Petrology and geochemistry of composite ultramafic xenoliths in alkali basalts and implications for magmatic processes within the mantle: American Journal of Science, v. 280-A, p. 389–426.

Karlstrom, K.E., and Humphreys, E.D., 1998, Persistent influence of Proterozoic accretionary boundaries in the tectonic evolution of southwestern North America: Interaction of cratonic grain and mantle modification events: Rocky Mountain Geology, v. 33, p. 161–179.

Keller, G.R., and Baldridge, W.S., 1999, The Rio Grande rift: A geological and geophysical perspective: Rocky Mountain Geology, v. 34, p. 121–130, doi: 10.2113/34.1.121.

Kogiso, T., Hirschmann, M.M., and Frost, D.J., 2003, High-pressure partial melting of garnet pyroxenite: Possible mafic lithologies in the source of ocean island basalts: Earth and Planetary Science Letters, v. 216, no. 4, p. 603–617, doi: 10.1016/S0012–821X(03)00538–7.

Kudo, A.M., Brookins, D.G., and Laughlin, A.W., 1972, Sr isotopic disequilibrium in lherzolites from the Puerco necks, New Mexico: Earth and Planetary Science Letters, v. 15, p. 291–295, doi: 10.1016/0012–821X(72)90175–6.

Lee, C.T.A., Cheng, X., and Horodyskyj, U., 2006, The development and refinement of continental arcs by primary basaltic magmatism, garnet pyroxenite accumulation, basaltic recharge and delamination: Insights from the Sierra Nevada, California: Contributions to Mineralogy and Petrology, v. 151, no. 2, p. 222, doi: 10.1007/s00410-005-0056-1.

Litasov, K.D., Foley, S.F., and Litasov, Y.D., 2000, Magmatic modification and metasomatism of the subcontinental mantle beneath the Vitim volcanic field (East Siberia): Evidence from trace element data on pyroxenite and peridotite xenoliths from Miocene picrobasalt: Lithos, v. 54, no. 1–2, p. 83–114, doi: 10.1016/S0024-4937(00)00016-5.

Liu, Y.S., Gao, S., Lee, C.T.A., Hu, S.H., Liu, X.M., and Yuan, H.L., 2005, Melt-peridotite interactions: Links between garnet pyroxenite and high-Mg# signature of continental crust: Earth and Planetary Science

Letters, v. 234, no. 1–2, p. 39–57, doi: 10.1016/j.epsl.2005.02.034.

Mayo, E., 1958, Lineament tectonics and some ore districts of the Southwest: American Institute of Mining Engineers Transactions, v. 10, p. 1169–1175.

McGetchin, T.R., and Silver, L.T., 1972, A crustal-upper mantle model for the Colorado Plateau based on observation of crystalline rock fragments in the Moses Rock dike: Journal of Geophysical Research, v. 77, p. 7022–7037.

McGuire, A.V., 1994, Southern Basin and Range Province crust-mantle boundary: Evidence from gabbroic xenoliths, Wikieup, Arizona: Journal of Geophysical Research–Solid Earth, v. 99, no. B12, p. 24,263–24,273, doi: 10.1029/94JB01184.

McGuire, A.V., and Mukasa, S.B., 1997, Magmatic modification of the uppermost mantle beneath the Basin and Range to Colorado Plateau Transition Zone: Evidence from xenoliths, Wikieup, Arizona: Contributions to Mineralogy and Petrology, v. 128, no. 1, p. 52–65, doi: 10.1007/s004100050293.

McMillan, N.J., Dickin, A.P., and Haag, D., 2000, Evolution of magma source regions in the Rio Grande rift, southern New Mexico: Geological Society of America Bulletin, v. 112, no. 10, p. 1582–1593, doi: 10.1130/0016-7606(2000)112<1582:EOMSRI>2.0.CO;2.

Mukhopadhyay, B., and Manton, W.I., 1994, Upper mantle fragments from beneath the Sierra Nevada batholith: Partial fusion, fractional crystallization, and metasomatism in a subduction-related ancient lithosphere: Journal of Petrology, v. 35, no. 5, p. 1417–1450.

New Mexico Bureau of Mining and Mineral Resources, 2000, Satellite Image of New Mexico: New Mexico Bureau of Mining and Mineral Resources Resource Map 23, scale 1:500,000.

Padovani, E.R., and Reid, M., 1989, Field guide to Kilbourne Hole maar, Doña Ana County, New Mexico, *in* Chapin, C. and Zidek, J., eds., Field excursions to volcanic terranes in the western United States, Volume 1: Southern Rocky Mountain region,: New Mexico Bureau of Mines and Mineral Resources Memoir 46, p. 174–179.

Pearson, D.G., and Nowell, G.M., 2004, Re-Os and Lu-Hf isotope constraints on the origin and age of pyroxenites from the Beni Bousera peridotite massif: Implications for mixed peridotite-pyroxenite mantle sources: Journal of Petrology, v. 45, no. 2, p. 439–455, doi: 10.1093/petrology/egg102.

Perkins, G.B., Sharp, Z.D., and Selverstone, J., 2006, Oxygen isotope evidence for subduction and rift-related mantle metasomatism beneath the Colorado Plateau–Rio Grande rift transition: Contributions to Mineralogy and Petrology, v. 151, p. 633–650, doi: 10.1007/s00410-006-0075-6.

Perry, F.V., Baldridge, W.S., and Depaolo, D.J., 1988, Chemical and isotopic evidence for lithospheric thinning beneath the Rio Grande rift: Nature, v. 332, no. 6163, p. 432–434, doi: 10.1038/332432a0.

Perry, F.V., Baldridge, W.S., Depaolo, D.J., and Shafiqullah, M., 1990, Evolution of a magmatic system during continental extension: The Mount Taylor volcanic field, New Mexico: Journal of Geophysical Research–Solid Earth and Planets, v. 95, no. B12, p. 19,327–19,348.

Pertermann, M., and Hirschmann, M.M., 2003, Partial melting experiments on a MORB-like pyroxenite between 2 and 3 GPa: Constraints on the presence of pyroxenite in basalt source regions from solidus location and melting rate: Journal of Geophysical Research–Solid Earth, v. 108, no. B2, p. 2125, doi: 10.1029/2000JB000118.

Prouteau, G., Scaillet, B., Pichavant, M., and Maury, R., 2001, Evidence for mantle metasomatism by hydrous silicic melts derived from subducted oceanic crust: Nature, v. 410, p. 197–200, doi: 10.1038/35065583.

Rapp, R.P., Shimizu, N., Norman, M.D., and Applegate, G.S., 1999, Reaction between slab-derived melts and peridotite in the mantle wedge: Experimental constraints at 3.8 GPa: Chemical Geology, v. 160, no. 4, p. 335–356, doi: 10.1016/S0009-2541(99)00106-0.

Riter, J.C.A., and Smith, D., 1996, Xenolith constraints on the thermal history of the mantle below the Colorado Plateau:

Geology, v. 24, no. 3, p. 267–270, doi: 10.1130/0091-7613(1996)024<0267:XCOTTH>2.3.CO;2.

Rudnick, R., McDonough, W.F., and Chappell, B.W., 1993, Carbonatite metasomatism in the northern Tanzanian mantle: Petrographic and geochemical characteristics: Earth and Planetary Science Letters, v. 114, p. 463–475, doi: 10.1016/0012–821X(93)90076-L.

Samuels, K., Brearley, A., and Selverstone, J., 2006, Metasomatic fluid compositions recorded by Cr-diopside pyroxenite xenoliths from the Colorado Plateau–Rio Grande rift transition zone: Eos (Transactions, American Geophysical Union), v. 87, abstract MR43C–1092.

Sapienza, G., Scribano, V., and Calvari, S., 2001, Kelyphitic breakdown of garnets from pyroxenite xenoliths, south-eastern Sicily, Italy: Periodico di Mineralogia, v. 70, no. 3, p. 377–386.

Sen, G., Keshav, S., and Bizimis, M., 2005, Hawaiian mantle xenoliths and magmas: Composition and thermal character of the lithosphere: The American Mineralogist, v. 90, no. 5–6, p. 871, doi: 10.2138/am.2005.1731.

Shaw, C.A., and Karlstrom, K.E., 1999, The Yavapai-Mazatzal crustal boundary in the Southern Rocky Mountains: Rocky Mountain Geology, v. 34, p. 37–52, doi: 10.2113/34.1.37.

Smith, D., 1979, Hydrous minerals and carbonates in peridotite inclusions from the Green Knobs and Buell Park kimberlitic diatremes on the Colorado Plateau, *in* Boyd, F., and Meyer, H.O.A., eds., The Mantle Sample: Inclusions in Kimberlites and Other Volcanic Rocks: Washington, DC, American Geophysical Union, p. 345–356.

Smith, D., 2000, Insights into the evolution of the uppermost continental mantle from xenolith localities on and near the Colorado Plateau and regional comparisons: Journal of Geophysical Research, v. 105, no. B7, p. 16,769–16,781, doi: 10.1029/2000JB900103.

Smith, D., and Barron, B.R., 1991, Pyroxene-garnet equilibration during cooling in the mantle: The American Mineralogist, v. 76, no. 11–12, p. 1950–1963.

Smith, D., and Griffin, W.L., 2005, Garnetite xenoliths and mantle-water interactions below the Colorado Plateau, southwestern United States: Journal of Petrology, v. 46, no. 9, p. 1901–1924, doi: 10.1093/petrology/egi042.

Smith, D., Riter, J.C.A., and Mertzman, S.A., 1999, Water-rock interactions, orthopyroxene growth, and Si-enrichment in the mantle: Evidence in xenoliths from the Colorado Plateau, southwestern United States: Earth and Planetary Science Letters, v. 165, no. 1, p. 45–54, doi: 10.1016/S0012-821X(98)00251-9.

Smith, D., Connelly, J.N., Manser, K., Moser, D.E., Housh, T.B., McDowell, F.W., and Mack, L.E., 2004, Evolution of Navajo eclogites and hydration of the mantle wedge below the Colorado Plateau, southwestern United States: Geochemistry, Geophysics, Geosystems, v. 5, doi: 10.1029/2003GC000675.

Stern, C.R., Kilian, R., Olker, B., Hauri, E.H., and Kyser, T.K., 1999, Evidence from mantle xenoliths for relatively thin (<100 km) continental lithosphere below the Phanerozoic crust of southernmost South America: Lithos, v. 48, no. 1–4, p. 217–235, doi: 10.1016/S0024-4937(99)00030-4.

West, M., Ni, J., Baldridge, W.S., Wilson, D., Aster, R., Gao, S., and Grand, S., 2004, Crust and upper mantle shear wave structure of the southwest United States: Implications for rifting and support for high elevation: Journal of Geophysical Research, v. 109, doi: 10.1029/2003JB002575.

Wilshire, H.G., Meyer, C.E., Nakata, J.K., Calk, L.C., Shervais, J.W., Nielson, J.E., and Schwarzman, E.C., 1988, Mafic and Ultramafic Xenoliths from Volcanic Rocks of the Western United States: U.S. Geological Survey Professional Paper 1443, 179 p.

Xu, Y.G., 2002, Evidence for crustal components in the mantle and constraints on crustal recycling mechanisms: Pyroxenite xenoliths from Hannuoba: North China: Chemical Geology, v. 182, no. 2–4, p. 301–322.